High-Throughput Microfluidic Capture of Rare Cells from Large Volumes of Blood

Joseph D'Silva

A Dissertation

Presented to the Faculty

of Princeton University

in Candidacy for the Degree

of Doctor of Philosophy

Recommended for Acceptance

by the Department of

Electrical Engineering

Adviser: Professor James C. Sturm

May 2016

Abstract

Deterministic lateral displacement (DLD) arrays are microfluidic devices capable of high-resolution separation of particles based on size. DLD arrays have been applied to separation of large cells from blood for a wide variety of diagnostic and analytical purposes. The volume of blood processed in these applications has been limited by volume-dependent performance degradation and throughput (volume/time) limitations. We address these issues in three ways in this thesis. First, we develop fabrication methods that increase the density of DLD arrays on a chip of a given area, resulting in an increase in the volumetric flow rate for a given pressure by a factor of ten. Second, we identify conventional platelet-driven clot formation as the source of the volume-dependent performance degradation and develop a method to completely inhibit clot formation in the DLD array, resulting in a 1000-fold increase in the volume of blood processed without device performance degradation. Third, we characterize the effect of post shape on the behavior of cells at high flow rates, corresponding to moderate Reynolds numbers (Re), by showing how post shape can be used to minimize shear-induced compression that reduces the target cell yield and to minimize hydrodynamic asymmetry that results in undesirable displacement of erythrocytes. Lastly, we finish by showing how post shape and row spacing can be used to minimize anisotropic conduction in DLD arrays that leads to non-ideal behavior of particles even at low Re.

Acknowledgements

To my parents.

Contents

List of Tables

List of Figures

Chapter 1

Introduction

1.1 Continuous Flow Separations

Separation of cells, functionalized beads, or other particles based on size, density, compressibility, or other properties is a critical step in many analytical and preparative techniques in medicine and biology [61]. These separations have traditionally been performed using bulk processes, such as filtration or centrifuge, which require more preparative steps and larger quantities of reagents. Microfluidic techniques offer a method of performing these separations more quickly, with better resolution, and using smaller quantities of reagents. These devices are fabricated using techniques borrowed from integrated circuit technology, and devices have been patterned in a variety of bulk materials, including silicon, glass, polymer, and plastics [61].

A wide variety of microfluidic techniques have been developed to perform such separations. All of these techniques rely on an effective force applied to the desired particles in a direction perpendicular to the flow, causing lateral displacement of a particle when the flow direction is defined as vertical. The magnitude of this displacement is dependent upon properties of the particle, such as size, density, compressibility, or charge. This spatial displacement of particles as the particles move

through the channel allows for both on-chip analysis of the spatial distribution of the particles and direction into separate outlet channels for off-chip analysis. For most applications involving high-throughput separations of cells from blood, three microfluidic techniques have been used: acoustic standing waves, inertial lift and Dean drag forces, and deterministic lateral displacement, which is the focus of this thesis.

Microfluidic separation techniques rely on laminar flow, which is the condition under which a particle will follow a streamline unless acted upon by an external force [67]. The flow is characterized by the Reynolds number Re, which is a dimensionless number used to characterize the ratio of inertial to viscous forces in the flow. It is defined as Re=ρvL/μ, where v and L are the characteristic velocity and length scale that describe the flow, ρ is the density of the fluid, and μ is the dynamic viscosity of the fluid. The flow is purely laminar up to Re of approximately 40, beyond which laminar flow is locally disrupted in certain regions due to vortex shedding. More relevant for the work in this thesis is Re$\sim$1, when inertial effects become important, causing changes in the flow pattern, up to Re of 20.

1.2   Continuous Flow Separation of Blood

The ability to separate cells in blood into distinct populations based on physical properties such as size or compressibility has numerous diagnostic and analytical applications [72]. In the case of epithelial tumor cells, it has been shown that increased deformability of the epithelial tumor cells correlates with increased metastasis [79]. Erythrocytes infected with malaria are approximately 50 times stiffer than erythrocytes that are not infected with malaria and have been isolated on this basis using microfluidic techniques [29]. Two major classes of microfluidic techniques have been used in separating cells in blood based on physical properties: active, which require an energy source input, and passive, which do not. We briefly discuss the major

achievements using techniques in each class in sorting cells in blood based on physical properties.

1.2.1   Passive Microfluidic Separation Techniques

Passive microfluidic separation techniques do not require an energy input to enable sorting and typically rely on properties of the flow within the microfluidic channel. Most applications involving high-throughput separations of cells from blood utilize three techniques: cross-flow filtration, inertial lift and Dean drag forces, and deterministic lateral displacement (DLD). Perfusion in continuous microfluidic cross-flow has been used to separate leukocytes from whole human blood [82]. Inertial lift forces, specifically the shear-gradient lift force and the wall lift force, cause certain cells to migrate to a fixed equilibrium distance away from the channel walls and have been used to separate cancer cells from blood on the basis of size and deformability [33]. High-throughput separation of cancer cells from blood has also been achieved using size-selective vortex technology and slanted-spiral microfluidics, both of which also rely on inertial lift and Dean drag forces to achieve separation (Dean drag forces relate to particle behavior in vortices which form perpendicular to the flow direction in sufficiently curved micro-channels.) [74, 83]. DLD has been used to separate blood into leukocytes, erythrocytes, and platelets and plasma, as well as for separation of specific cell types from whole blood for a wide variety of diagnostic applications, which we discuss later in this chapter [14].

1.2.2   Active Microfluidic Separation Techniques

We define active microfluidic separation techniques as those which require an energy input to enable sorting or require the attachment of a functionalized label to the desired particles. Some active microfluidic separation techniques, such as dielectrophoresis, magnetic-force-based sorting, and optical trapping, require the attach-

ment of functionalized beads with specific properties to enable the separation of cells from blood [72]. Micro-fabricated magnetic stripes in the bottom of a micro-channel have been used to separate leukocytes, which had been selectively labelled with magnetic nanoparticles, from whole blood [38]. In contrast, separation using acoustic standing waves is typically label-free and depends only on the relative densities and compressibilities of the particles and the carrier medium. Acoustic standing waves have been used to transfer erythrocytes from contaminated plasma to clean plasma in a microfluidic channel [64].

1.3 Deterministic Lateral Displacement: Principles of Operation

Deterministic lateral displacement (DLD) arrays are microfluidic devices that offer continuous-flow separation of particles suspended in a fluid based on size. The mechanism of action is that suspended particles in a fluid that are larger than a critical size experience sequential displacement (bumping) from one streamtube to an adjacent one in a direction perpendicular to the flow by micro-posts that are arranged in a tilted rectangular or parallelogram array [30]. Particles smaller than this critical size travel in the average flow direction, while particles larger than this critical size travel at the array tilt angle.

Figure 1.1 is a schematic showing the relevant parameters and typical particle behavior. The critical size is a function of the gap, G, and the array tilt angle $\epsilon = d/\lambda$ [35]. The tilt angle, ϵ, is typically chosen such that $1/\epsilon$ is an integer. For circular posts, the diameter of the post is typically set equal to the gap, G. The array shown in Figure 1.1 uses a parallelogram unit cell, although the tilt can also be achieved using an array with a tilted rectangular unit cell. Since there can be no
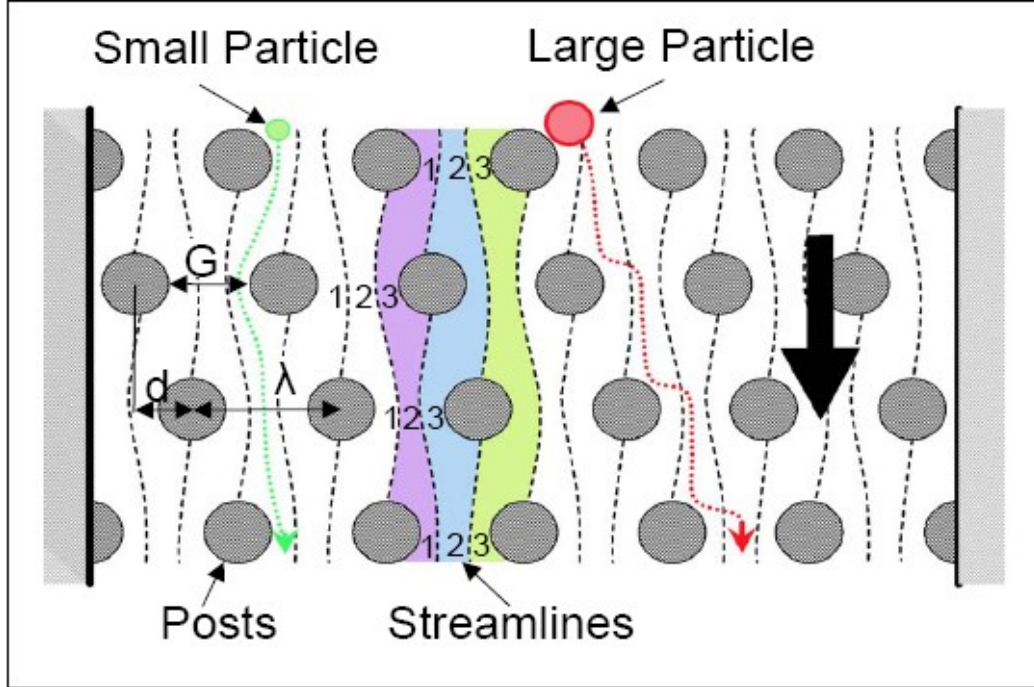
Figure 1.1: Schematic showing the separation of a large particle from a small particle via a DLD array with a row-shift fraction of one-third. The row-shift fraction (ϵ=d/λ) divides the flux in the gap (G) between the posts into $1/\epsilon$=3 streamtubes, which are divided by streamlines. Large particles, defined as particles larger than the width of the first streamtube next to the post on the side of the post that displaces the particle, are displaced by the post with each subsequent row in the direction of the flow, traveling at the array tilt angle over the course of many rows of posts. Small particles, defined as particles smaller than the width of the first streamtube next to the post on the side of the post that displaces the particle, follow the streamtube, traveling in the average fluid flow direction over the course of many rows of posts (illustrated by the black arrow). Image courtesy of J.A. Davis et al. [14].

fluid flux into the walls, the fluid flow is on average strictly vertical, as shown by the black arrow in Figure 1.1.

The device works by asymmetric bifurcation of the fluid streams around the posts. The array tilt angle, ϵ, divides the flux in the gap, G, between the posts into $1/\epsilon$ streamtubes. $1/\epsilon$-1 of these streamtubes pass through the next gap, while the remaining streamtube passes around the opposite side of the next post. These streamtubes are separated by stagnation streamlines that begin and end on posts and show how the fluid divides around the posts.

Particles in the flow behave in one of two ways depending upon the size of the particle relative to the size of the first streamtube next to the post on the side of the post that displaces the particle. If the radius of the particle is larger than the width of the streamtube next to the post, the particle will be bumped by the post into the adjacent streamtube. If the radius of the particle is smaller than the width of the streamtube next to the post, the particle will remain within the current streamtube and follow a zigzag trajectory as it travels through the array. Because of the cyclical way the streamtubes move through the gaps, large particles travel at the tilt angle of the array while small particles follow the average flow direction, which is vertical.

The critical size separating large particle behavior from small particle behavior can be predicted using a method developed by D. Inglis et al. [35]. The flux in the gap is divided into $1/\epsilon$ streamtubes of equal volume flux, and the critical particle radius is the width of the streamtube next to the post on the side of the post which bumps the particle. This can be found by simple integration over the velocity profile in the gap.

Post geometry can be used to alter the velocity profile in the gap therefore also the critical size. K. Loutherback et al. showed that asymmetric triangular posts allow for a 50% larger gap for a given critical size and tilt angle [49]. Asymmetric triangular posts can also be used to achieve a different critical size in the same array for opposite flow directions [51]. The effect of post shape is investigated in detail in Chapter 4.

Because deterministic lateral displacement relies only on particles following streamlines unless displaced by posts, the separation is independent of flow velocity as long as the flow remains laminar to first order. At Re>1, even if the flow is laminar, several second order effects can affect DLD array performance. These are discuss in Chapter 4 and include inertial effects affecting the fluid flow and particle paths and effects of the fluid flow on the particle shape and orientation. To first

6

order, the separation resolution is enhanced by increased flow velocity, since increased flow velocity allows less time for diffusion [30]. Compared to acoustic and inertial microfluidic cell sorting techniques, deterministic lateral displacement does not have a minimum channel length that depends on flow velocity.

The capabilities of DLD arrays have been expanded through use in combination with active microfluidic separation techniques. Dielectrophoresis has been used to allow tunability of the critical size in DLD arrays, which is typically determined purely by hydrodynamic conditions [5]. An electrode-based virtual pillar array which combined DLD with dielectrophoretic effects has been used to achieve 99% separation of leukocytes from erythrocytes [8]. The DLD concept has also been extended using interdigital transducers to create acoustic standing waves at an angle to the average flow direction, which allows size-based separation of particles [12].

1.4   Deterministic Lateral Displacement: Applications toward Separation of Nucleated Cells from Blood

Table 1.1: Physical characteristics and concentrations of the major components in whole adult human blood.

Cell Type	Cell Shape	Diameter (μm)	Concentration (mL^{-1})
Platelet	Various	1-5	5.0-10.0x10^7
Erythrocyte	Biconcave Discoid	2x7.5	4.0-5.5x10^9
Leukocyte	Spheroid	5-20	4.0-10.0x10^6

Blood contains cells that range in size from 1μm to 20μm, with the size of a cell often being related to its biological function. With a critical size that is set by design parameters, DLD arrays are well suited to separating blood into its main components

of leukocytes, erythrocytes, and platelets [14]. The sizes and concentrations of these components in whole adult human blood are shown in Table 1.1.

DLD arrays have been applied to the capture of variety of rare cells of biological interest from whole blood. Compared with other microfluidic techniques, the major advantage of DLD arrays in these applications is the ability to capture these rare cells without the background of erythrocytes present in whole blood [40]. D.W. Inglis et al. demonstrated that DLD arrays can be used to separate malignant lymphocytes from healthy lymphocytes [36]. L.R. Huang et al. have used DLD arrays to capture nucleated red blood cells from the peripheral blood of pregnant women for applications in prenatal diagnostics [32]. S.H. Holm et al. have used DLD arrays to separate parasites from human blood [26]. B. Zhang et al. have used DLD arrays to separate cardiomyocytes from blood [91]. Typical volumes of blood processed for such applications have been limited to 100 μL per DLD array due to volume-dependent performance degradation.

While the capture efficiencies achievable with DLD arrays are sufficiently high to be useful in rare cell capture (>85%), the volumes of blood processed in the previous examples were small (<100 μL). This is insufficient for many diagnostic purposes. To process large volumes of blood, high-throughput operation of DLD arrays for capture of cancer cells from blood has recently been demonstrated. K. Loutherback et al. have demonstrated capture of greater than 85% of cancer cells from diluted whole blood at flow rates as high as 10 mL/min (Figure 1.2) [50]. Z. Liu et al. demonstrated capture of cancer cells from diluted whole blood at similar flow rates and showed that capture rates remain high at these high flow rates with DLD arrays using triangular posts but decrease with increasing flow rate for DLD arrays using circular posts [47]. However, both of these experiments still only processed small volumes of blood (<200 μL per DLD array).
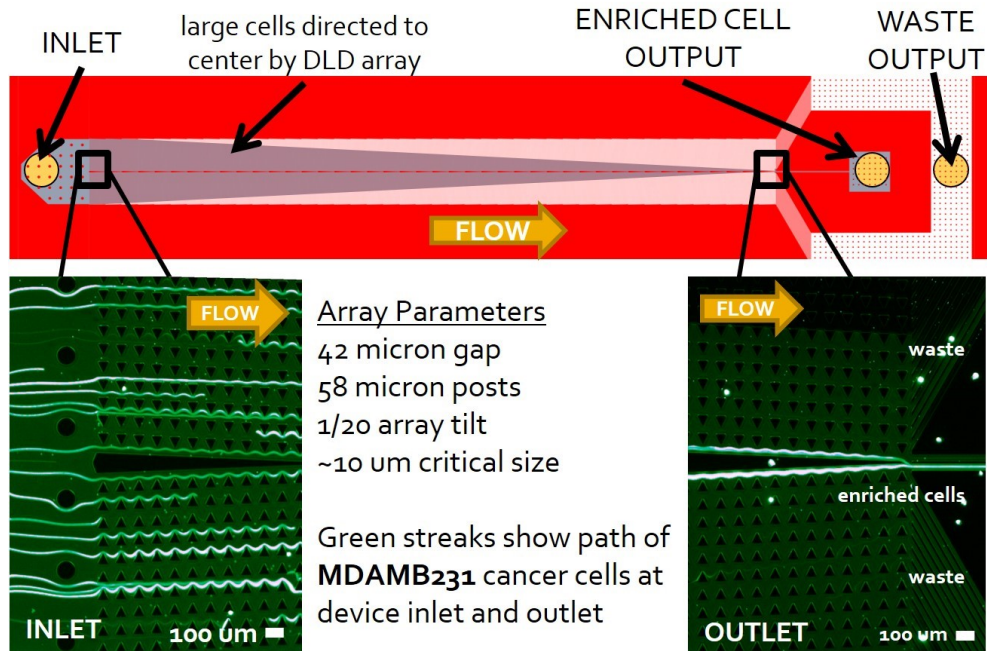
Figure 1.2: Concentrator DLD array used to achieve high-throughput (10 mL/min) enrichment of cancer cells from blood. The path of the MDAMB231 cancer cells are shown as green streaks. The cells are evenly distributed across the entire width of the array at the inlet and are concentrated into the center of the array at the outlet. (Figure courtesy of K. Loutherback.)

1.5 High-Throughput, High-Volume Separation of Cells from Blood using DLD Arrays

This thesis aims to set the foundation for using DLD arrays to process large volumes of blood (10-100 mL). Two potential applications are the capture of circulating tumor cells (CTCs) and harvesting of stem cells. First, CTCs have been identified in the blood of patients with metastatic disease and can be used to assess the severity of disease and the effectiveness of various treatment strategies [13]. CTCs can be isolated from blood using DLD arrays since these cells typically have diameters of 15 to 30 μm, with only slight overlap in the size distribution with leukocytes [58]. Second, there are a number of applications involving isolation of leukocytes and cells similar in size to leukocytes from whole blood. One particularly interesting application is the

isolation of hematopoietic stem cells (HSCs), which are similar in size to leukocytes, from umbilical cord blood (UCB) [75]. Currently, isolation of HSCs from UCB is achieved using centrifugation technology, which has limited resolution resulting in loss of HSCs and contamination by erythrocytes and involves large amounts of reagents. We examine separation of leukocytes from whole blood as a model system for isolation of HSCs from UCB.

Both of these applications require processing 10-100 mL of blood. CTC concentrations in the blood of patients with metastatic cancer can be as low as 1-10 mL^{-1}, typically requiring processing of $\sim$10 mL of blood for diagnostic applications [71]. UCB is collected in volumes of 50-100 mL [78], and maximizing the stem cell yield requires processing this entire volume.

Applications of DLD arrays toward separation of cells from large volumes of blood (10-100 mL) face two major limitations. First, while the flow rates at which DLD arrays can be operated has increased by a factor of 10^5, the volume of blood that can be processed with DLD arrays has not increased by a similar factor due to clot formation in the array. Increasing the volume of blood that can be processed with DLD arrays requires identifying and inhibiting the mechanisms driving this clot formation. Inhibition of clot formation in DLD arrays will also allow for collection of target cells in a buffer stream without the background of erythrocytes and platelets present in blood. This is not possible with the concentrator design that has been used for high-throughput enrichment of cancer cells from blood with DLD arrays [50, 47].

Second, the behavior of cancer cells, leukocytes, and erythrocytes at high flow rates has not been well characterized in two ways. The behavior of erythrocytes at high flow rates in DLD arrays is important because a major advantage of DLD arrays over other microfluidic technologies is the ability to separate nucleated cells without the background of erythrocytes present in whole blood. For nucleated cells, such as cancer cells and leukocytes, the main concern with high throughput operation of DLD

arrays is minimizing shear-induced reduction in size of the cell, so that a high capture efficiency based on displacement of cells above the critical size of the DLD array can be maintained. Overcoming these two limitations will allow for high efficiency separation of nucleated cells from large volumes of whole blood using DLD arrays.

1.6   Thesis Outline

Chapter 2 details the experimental methods and setup for high-throughput operation of DLD arrays. We introduce three fabrication processes that increase the density of DLD arrays in a given chip area by a factor of 4. Two of the three fabrication processes increase the maximum depth of the DLD arrays by a factor of 2.5, yielding a 10-fold increase in volumetric flow rate for a given pressure over that which was achievable using previous fabrication processes. We also introduce a bubble-free manifold design for operating the high-throughput manifold over long times to process large volumes. Lastly, we introduce the imaging setup and cell labelling techniques utilized for the experiments in Chapter 3.

Chapter 3 demonstrates the inhibition of clot formation, removing a key limitation to processing large volumes of blood using DLD arrays. We identify that clot formation occurs dynamically at the beginning of the array and is not due to clots that form in the tubing leading to the chip. We then show that platelets, not leukocytes or erythrocytes, are the driver of this clot formation, and we examine the biological and physical mechanisms that contribute to clot formation. We then show that the activity of calcium ions and thrombin are the dominant mechanisms driven clot formation. We inhibit these mechanisms and show that this method of inhibition is effective at both high and low flow rates and correspondingly high and low shear rates.

Chapter 4 discusses the effects of post geometry on the behavior of erythrocytes and leukocytes in DLD arrays at high flow velocities (moderate Re: 1<Re<20). First, we examine the effect of post geometry on the extent of cell deformation against the micro-posts at high flow rates. We show that the extent of cell deformation is directly related to the shear at the post surface against which the cell can be deformed resulting from fluid bending around the post. Second, we examine the flow velocity dependent erythrocyte contamination of the product that occurs with asymmetric triangular posts but not with circular posts in DLD arrays with shallow tilt angles (tilt < 1/20). Using eight different post geometries, we show that the extent of erythrocyte contamination of the product at high flow velocities is directly related to the asymmetry of the fluid centripetal acceleration distribution in the gap. Finally, we combine the results of these two sets of experiments to achieve high yield separation of leukocytes from blood with minimal erythrocyte contamination using a DLD array with diamond-shaped posts.

Chapter 5 examines the effect of post geometry on anisotropic conduction in the DLD array at low Re. Anisotropic conduction in DLD arrays, which causes a misalignment of the pressure gradient to the average flow direction, can be caused by either a rhombic (not tilted square) unit cell array or by post shapes that are asymmetric. We first examine how the tilt of the array and post geometry contribute to anisotropic conduction. We then show that anisotropic conduction can be minimized by increasing the spacing between the rows in the direction of the flow.

Chapter 6 summarizes our contributions and makes suggestions for future work in this area.

Chapter 2

High-Throughput Deterministic Lateral Displacement Array Experimental Setup

2.1 Introduction

In this chapter, we cover the major components of the experimental setup for operating high-throughput deterministic lateral displacement arrays. First, we develop fabrication techniques to increase the channel depth and density of DLD arrays on a chip of a given size. We then develop a manifold through which fluidic connections are made to the chip that can be operated at high pressures and is resistant to the formation of bubbles that can form when operating the DLD arrays for long times to process large volumes. We then present the imaging setup used to visualize beads, leukocytes, and cancer cells in the DLD array.

2.2 Parallelization of Deterministic Lateral Displacement Arrays for High-Throughput Processing of Blood
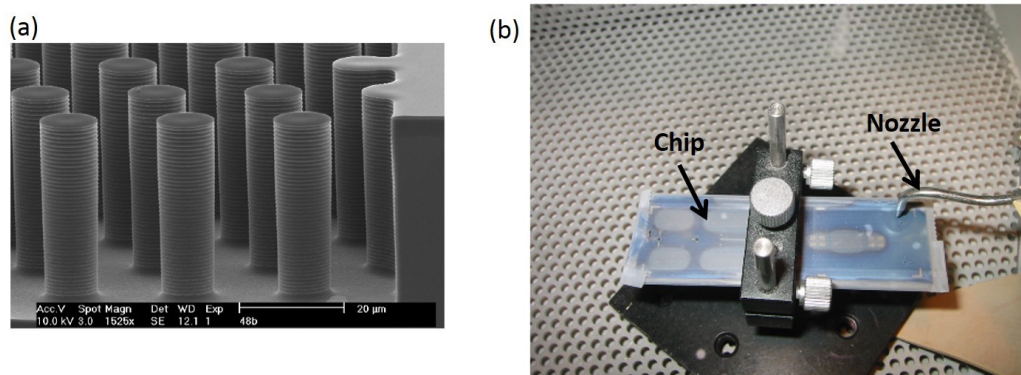
Figure 2.1: (a) SEM image of a DLD array etched into silicon using deep reactive ion etching (DRIE). Image courtesy of Keith Morton. (b) Setup for sandblasting through-holes, through which fluid enters and exits the chip. Limitation in the precision of the through-hole size and positioning of the nozzle limit the number of DLD arrays that can fit in a given area. Image courtesy of David Inglis.
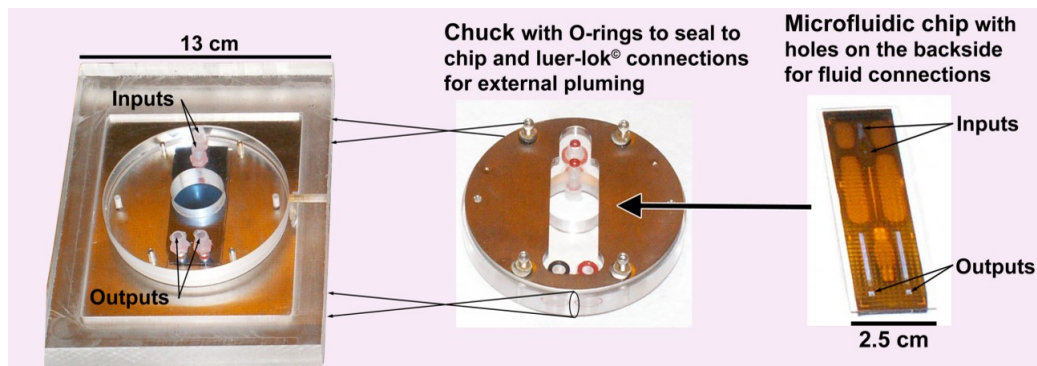
Figure 2.2: The through-holes of the DLD array chip mate via O-rings to an acrylate manifold, through which fluidic connections are made to the DLD array chip. Image courtesy of David Inglis.

Deterministic lateral displacement (DLD) arrays with deep channels (depth>10 μm) have traditionally been fabricated in silicon using deep reactive ion etching

(DRIE) (Figure 2.1(a)). Through-holes through which fluid enters and exits the chip have traditionally been created via sand-blasting (Figure 2.1(b)). The through-holes of the DLD array chip mate via O-rings to an acrylate manifold, through which fluidic connections to the DLD array chip are made(Figure 2.2). The lack of precision in size and placement of the through-holes made via sand-blasting limits the number of DLD arrays that can be placed in a given area on a silicon chip. For this reason, a typical 1.5-mm wide DLD array requires approximately 8 mm width on the silicon chip. We present three techniques that overcome this limitation: (i) a technique using an oxide layer for pattern transfer that allows two patterns to be etched into a single side of a silicon wafer, one of which is for precisely placed through-holes, (ii) a technique using backside alignment that allows etching of two patterns, one of which is for precisely placed through-holes, into a silicon wafer by first performing photolithography and etching one side of the wafer and then performing the same on the opposite side of the wafer, and (iii) a technique that utilizes a powerful laser with alignment capability to within 10 μm and size control to within 25 μm to blast the through-holes. These three techniques allow for fitting a typical 1.5-mm wide DLD array in approximately 1.6-mm width on a silicon chip.

2.2.1 Oxide Mask Technique: All Front-Side Processing

The sandblasted through-holes, with the required spacing to compensate for the lack of precision in size and placement, cause a typical 1.5-mm wide DLD array to require approximately 8-mm width on a silicon chip. In principle, with anisotropic deep reactive ion etching, we could etch through-holes patterned via photolithography such that a typical 1.5-mm wide DLD array would require only 1.6-mm width on the silicon chip, a reduction in area of a factor of five. A challenge however occurs when the micro-post array is etched first. In trying to spin a 7 μm thick layer of AZ4330 photoresist over the micro-post array, which is typically etched to a depth greater than
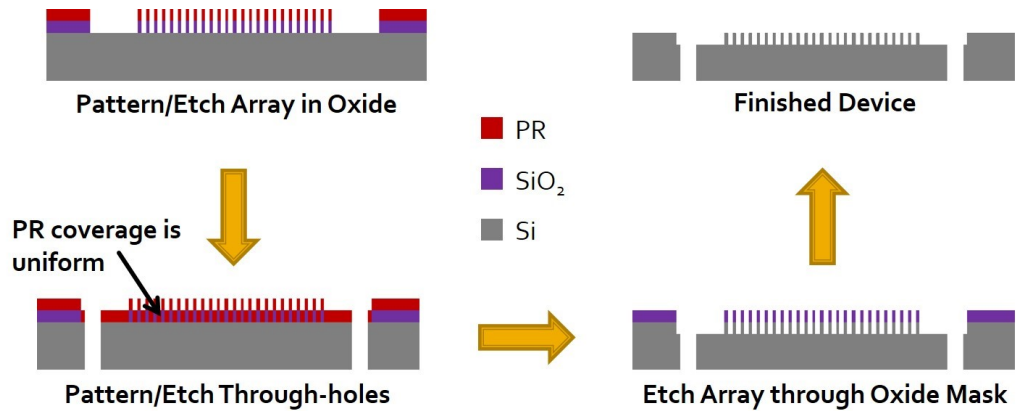
Figure 2.3: Cross-sections of major steps in the fabrication process that uses an oxide mask to achieve etching of two aligned patterns on the front side of a silicon wafer.

60 μm, the photoresist coverage is non-uniform. When we etch the through-holes, the regions that are not covered by photoresist due to the non-uniform coverage are also etched through along with the through-holes, resulting in randomly placed holes through the array.

Oxide masks have been used for pattern transfer in the fabrication of micro-electro-mechanical systems (MEMS) devices [65]. We grow an oxide with thickness of 1.2 μm using a wet oxidation process. Using a standard deep reactive ion etch (DRIE) Bosch process, the selectivity between the oxide and silicon is such that 80 μm of Si can be etched for each 1 μm thickness of the oxide mask. For comparison, 100 μm of Si can be etched for each 1 μm of thickness in AZ4330 photoresist mask using the same etch recipe.

The major steps involved in this fabrication process are shown in Figure 2.3. The micro-post array is first patterned in a 1.4 mum thick layer of AZ5214 photoresist. The pattern is then transferred to the oxide using a buffered oxide etch (BOE). A 7 μm thick layer of photoresist is then spun on top of the patterned oxide layer. The photoresist coverage is uniform now because we are spinning a 7 μm thick layer of photoresist on top of a patterned surface with 1.2 μm depth instead of 60 μm

depth (Figure 2.3), as we attempted to do in the process without the oxide mask. The through-holes are then etched using the 7 μm thick photoresist as a mask. This photoresist mask is then removed, and the micro-post array is etched through the oxide mask to a depth of 80 μm.

With this process, we can etch through-holes as small as 100 μm by 100 μm squares through a standard 550 μm thick 4-inch wafer. Minimum spacing between through-holes is 500 μm. We successfully fabricate a 70-mm by 36-mm chip containing 18 DLD arrays with 108 through-holes of 100 μm by 100 μm size using this process.

The major drawback of this process is that the 1.2-μm oxide mask was etched isotropically using BOE. This results in the size of the micro-posts being reduced in size by an amount equal to the thickness of the oxide. While this can be easily compensated for in the case of circular posts, it can also affect the sharpness of post geometries with corners, such as triangles. This reduction in sharpness can have a significant effect on critical size [49]. Possible future work could use an anisotropic dry etch of the oxide layer.

2.2.2   Backside Alignment Technique
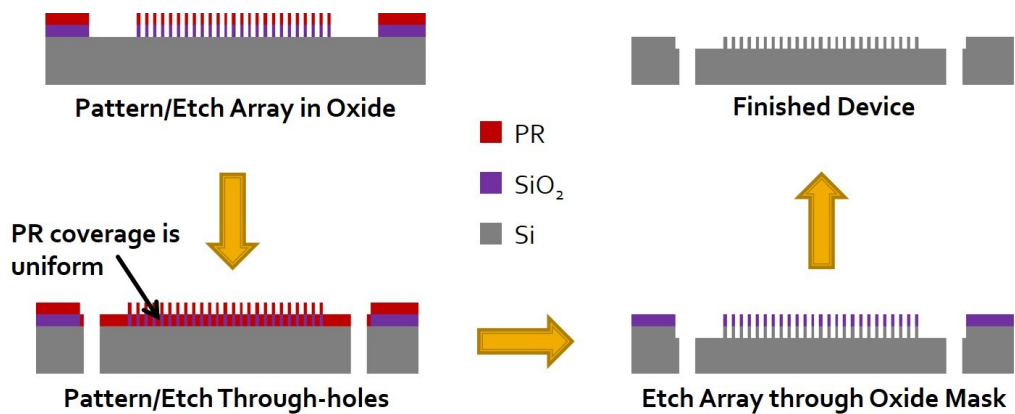
Figure 2.4: Cross-sections of the major steps in the fabrication process that uses backside alignment to pattern and etch the micro-post array on one side of the wafer while through-holes are patterned and etched from the other side of the wafer.

Silicon is nearly transparent for near infrared light. This allows for a mask alignment technique in which a pattern in photoresist on one side of a wafer can be aligned to features that have been etched into the opposite side of the wafer. Alignment is easier if the depth to which features have been etched on the opposite side of the wafer is large, since contrast is achieved through thickness-dependent absorption of the infrared light by the silicon wafer. Here, we use this backside alignment technique to pattern through-holes in photoresist aligned to a micro-post array that has been etched into the opposite side of the wafer.

The major steps involved in this fabrication process are shown in Figure 2.4. A 3 μm thick layer of AZ4330 photoresist is spun onto one side of a double-side polished silicon wafer. The micro-post array is patterned and etched to a depth of 160 μm. A 7 μm thick layer of AZ4330 photoresist is then spun onto the opposite side of the wafer. A specially designed chuck that elevates the wafer above the surface of the chuck so as not to scratch the features that have been etched into the opposite side of the wafer is used in spinning on the photoresist. The pattern for the through-holes is then aligned to the micro-post array etched on the opposite side of the wafer using a mask aligner equipped with an infrared light source and camera. The through-holes are then etched using a standard anisotropic etch (Bosch) process. Details of this fabrication process can be found in Appendix B.

This fabrication process overcomes two major limitations imposed by the previous process. First, the limitation on etch depth achievable for the micro-post array is limited by the maximum aspect ratio at which the micro-posts can remain standing, which is approximately 10:1, not by the thickness of the mask through which the micro-post is etched. Second, the dimensions of the micro-posts are identical to the mask pattern, whereas with the oxide mask process, the dimensions of the micro-posts were affected by the isotropic etching of the oxide mask. These are the two main practical differences between the two techniques.

2.2.3 Laser Cutting Technique

Patterning through-holes using the backside alignment technique and the oxide mask technique can be challenging due to non-uniformities in the photoresist layer caused by particles in the photoresist (We seek to make "perfect" devices over 36 mm by 70 mm area.). Instead of using a Bosch process to etch through the wafer, we use a powerful YAG laser to cut through-holes as small as circles with 100μm diameter. Although our system is not set up for alignment to automate the positions at which through-holes are cut, commercial systems can be programmed to achieve this with positional precision as high as 10μm. We use this technique to rapidly fabricate chips with a single channel, requiring only six through-holes, for testing the effects of different post geometries in Chapters 3 and 4 of this thesis.

2.3 Sealing of the Micro-Post Array

Sealing of the micro-post array is important in high-throughput applications for two reasons. First, any irregularities in the sealing layer cause distortions in the flow pattern, which can cause displacement of particles below the critical size. Second, the sealing layer needs to be able to withstand high pressure. It has also been shown that a sealing layer with a high Young's modulus, such as the Pyrex glass slides used in anodic bonding, makes the flow less sensitive to fluctuations caused by the syringe pump [90].

2.3.1 Pressure-Sealing Tape

Before sealing with the pressure-sealing tape, the chip is cleaned using a standard Piranha clean and then exposed to an oxygen plasma so that the surface is made hydrophilic. The Piranha clean begins with immersing the chip in a 1:1 mixture of 96% sulfuric acid and 30% hydrogen peroxide for 15 minutes. The chip is then
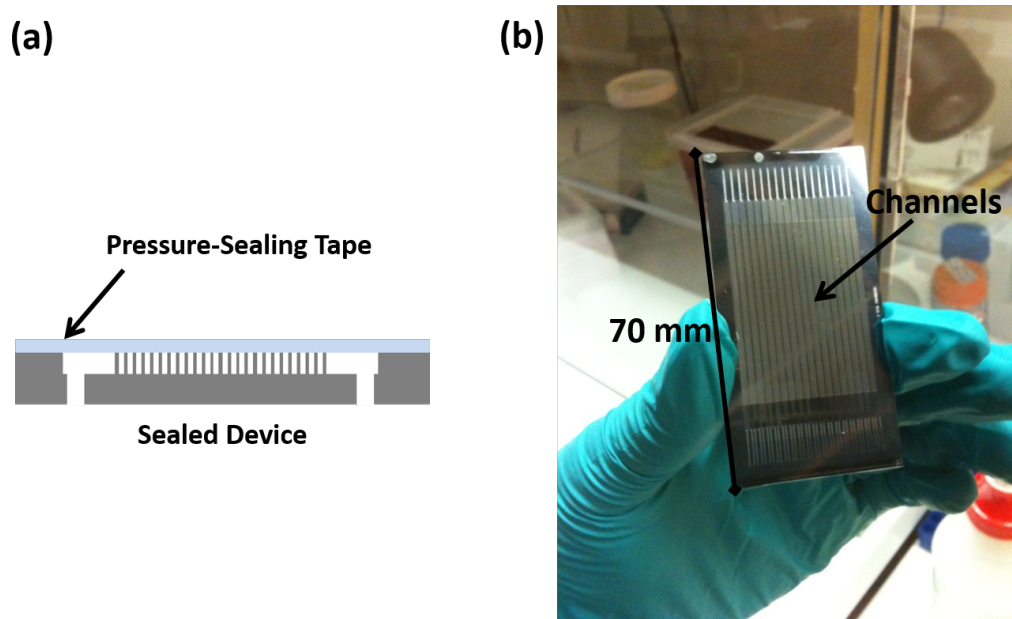
Figure 2.5: (a) Schematic of a DLD array sealed with pressure-sealing tape. (b) Silicon chip with 18 DLD arrays in parallel sealed with pressure-sealing tape. Bubbles formed in bringing the tape and silicon chip together are pushed toward the edge of the chip away from the array using a rubber rolling pin.

rinsed with DI water and dipped in 2% hydrofluoric acid for 1 minute. The chip is rinsed with DI water and then dried under nitrogen. In order to make the surface hydrophilic, the chip is exposed to a 1kW oxygen plasma for 90s.

Compared to a thin PDMS layer backed by a glass slide, which is the method previously used to seal DLD arrays, the pressure-sealing tape (9795R, 3M Co.) contains fewer defects that can cause deviations in the flow pattern in the chip. The backing from the pressure-sealing tape is removed, and the tape is positioned on top of the chip with no pressure applied. A rubber rolling pin is then used to seal the tape to the chip without any bubbles in the array region. Compared to the depth to which the chip is etched, there is negligible caving of the tape into the array (Figure 2.5).

One advantage of the pressure-sealing tape is that it can be easily removed to enable cleaning and re-use of the chip. To remove the tape, the sealed chip is first soaked for roughly two days in acetone. A razor is then used to lift the tape from

the corner of the chip, creating a tab. Using this tab, the tape can be easily peeled from the chip before the acetone evaporates. If the acetone evaporates before peeling is completed, the chip can be simply re-dipped in acetone before peeling of the tape is continued.

This method has been used at pressures as high as 50 psi without leaking. However, at pressures above 10 psi, the tape can detach from the chip in certain regions over the array, causing irregular behavior of particles in the array. Therefore, anodic bonding of Pyrex lids was investigated (Section 2.3.2). All of the experiments involving imaging were conducted using DLD arrays sealed with pressure-sealing tape.

2.3.2   Anodic Bonding

We use air anodic bonding to attach a Pyrex lid to the silicon chip into which the DLD array has been etched. The surface properties of the Pyrex slide and silicon chip are extremely important in successfully achieving anodic bonding since the bonding is due to the forces between opposite charges that are driven towards the interface between the Pyrex slide and silicon chip [45]. The Pyrex slide is cleaned by immersion for 15 minutes in a 1:1 mixture of 96% sulfuric acid and 30% hydrogen peroxide. The silicon chip is cleaned in the same way as the Pyrex slide with an additional step. To remove the native oxide from the surface of the silicon chip, the chip is immersed for 90s in 2% hydrofluoric acid. The Pyrex slide and silicon chip are pushed together without being blown dry and mounted in the holder shown in Figure 2.6, which is used to align the two pieces for bonding. The holder with the Pyrex slide and silicon chip mounted are kept under water until anodic bonding is performed to prevent oxidation of the surface of the silicon chip.

The setup for anodic bonding is shown in Figure 2.6. The holder with the Pyrex slide and silicon chip are removed from under water and placed on the hot plate. A piece of graphite is placed on top of the Pyrex slide, and the voltage probe is placed
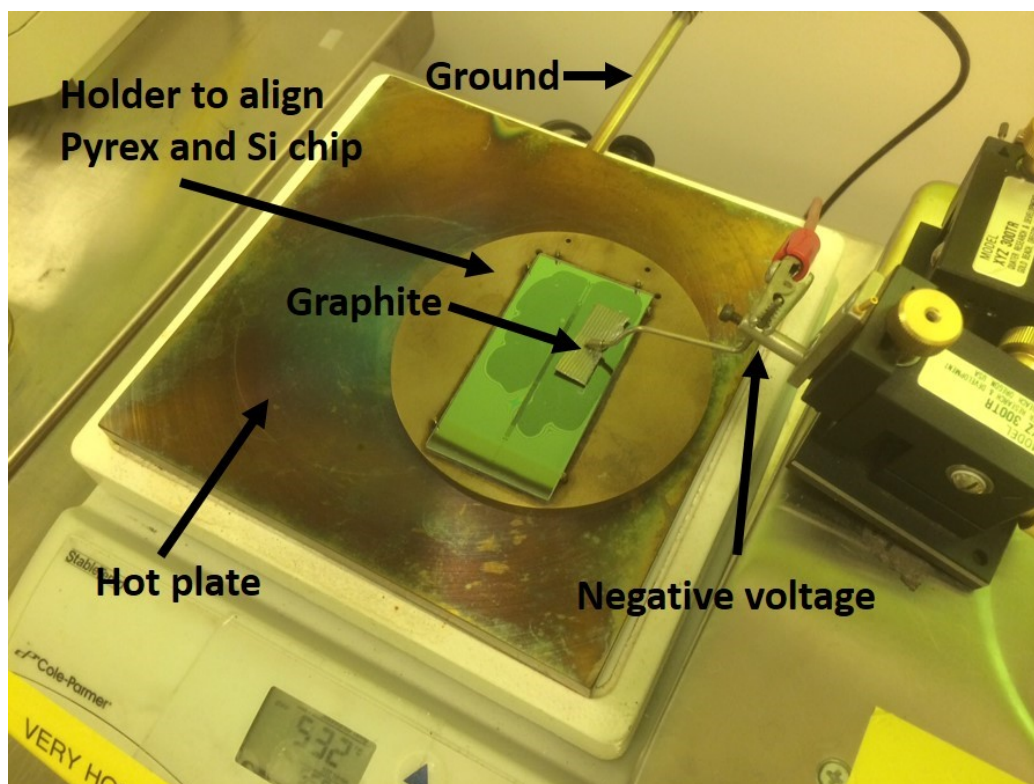
Figure 2.6: Setup for anodically bonding a Pyrex glass slide to a silicon chip into which a DLD array has been etched. A voltage of -1000V is applied on top of the Pyrex slide through a probe connected to the Pyrex slide through a piece of graphite, which is simply placed on top of the Pyrex slide. The base of the hot plate is grounded. The Pyrex slide and silicon chip are placed on top of a stainless steel holder to align the two pieces. Anodic bonding is performed at a temperature above 500°C in air.

on top of this piece of graphite. Alignment between the silicon chip and Pyrex in the holder is checked. Both the Pyrex slide and silicon chip are still wet at this point. The hot plate is then set to 550°C, and the temperature is allowed to stabilize over 30 minutes. The voltage, set at -1000V, is then turned on. As bonding proceeds, the dark region shown in Figure 2.6 expands to eventually cover the entire area of the chip. Once bonding is complete, the hot plate is turned off, while the voltage is left on as the chip cools to prevent detachment of the bond due to uneven thermal shrinking of the Pyrex slide and silicon chip. The voltage is turned off once the hot

plate reaches a temperature of 50°C. For safety, the voltage supply is operated with a current trip set to 5 mA.

2.4   Bubble-Free, High-Pressure Manifold Design
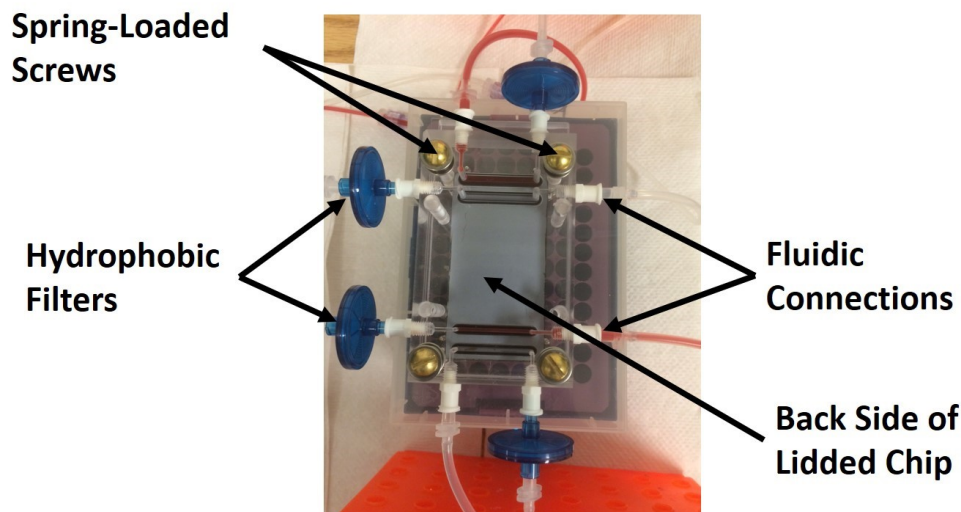
Figure 2.7: Acrylic manifold for fluidic connections to a lidded silicon chip into which the DLD arrays have been etched. The through-holes on the silicon chip align to reservoirs in the manifold. Each reservoir is connected on one side to a fluidic connection and on the other side to a hydrophobic filter, which is used to prevent bubbles from entering the chip. Spring-loaded screws evenly distribute the pressure onto the O-rings surrounding the reservoirs, allowing for operation at high pressures.

The silicon chip is mounted into an acrylic manifold to which fluidic connections are made (Figure 2.7). This manifold has two advantages over manifolds that have been used previously. First, it is made resistant to bubbles forming in the reservoirs in the manifold by connecting each reservoir to both a fluidic connection and a hydrophobic filter, through which bubbles can exit. Second, it uses spring-loaded screws to evenly distribute the pressure to the O-rings that surround each reservoir, making it possible for the manifold to be used at pressures as high as 50 psi.

Prior to the experiment, the manifold is thoroughly rinsed with DI water and blown dry with nitrogen. The manifold is then heated overnight at 40°C to drive

off any remaining moisture. The O-rings are then placed around the reservoirs, the sealed chip is mounted, and the top plate is screwed onto the manifold, pressing the chip onto the O-rings. As shown in Figure 2.7, hydrophobic filters are attached to the white luer fittings extending from the manifold, and barbed-luer fittings are used to connect peroxide-cured silicone tubing to the remaining white luer fittings extending from the manifold.
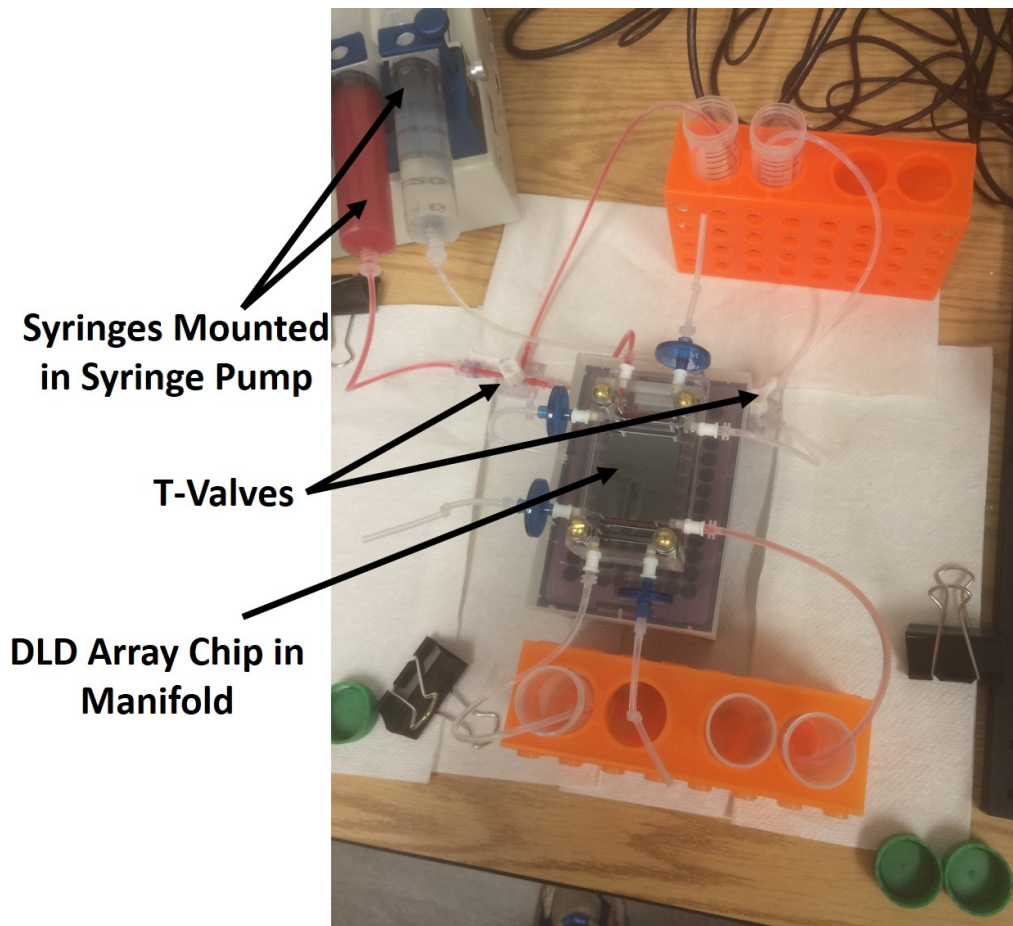
Figure 2.8: A dual-input syringe pump is used to drive the sample and buffer inputs of the bubble-free, high-pressure manifold. T-valves are used to release bubbles in the tubing connecting the syringes to the manifold.

A dual-input syringe pump is used to drive the sample and buffer inputs of the bubble-free, high-pressure manifold(Figure 2.8). T-valves are used to release bubbles that may have formed in the tubing connecting the syringes to the manifold and to

enable changing of the syringes driving the inputs to the manifold. In order to ensure complete wetting of the tubing, manifold reservoirs, and DLD array chip, wetting is performed using a single syringe containing 2% Pluronic F108 surfactant in DI water. 60 mL syringes containing the sample and buffer are loaded following wetting, making use of the T-valves to avoid the introduction of bubbles into the reservoirs in the manifold. A detailed list of the parts required to assemble the setup shown in Figure 2.8 can be found in Appendix C.

2.5 Imaging Setup and Fluorescent Labelling of Cells

In this section, we describe the setup we use to image cells in the DLD array and the procedures we use to fluorescently label the cells for imaging.

2.5.1 Imaging Setup

A green fluorescent protein (GFP) filter set is used with a blue LED source (470 nm) to image appropriately labelled particles or cells. Blue light from the LED source is reflected off the dichroic mirror onto the DLD array chip. The emitted fluorescence from the cells or particles in the DLD array then passes through the dichroic mirror and then through a lens to the camera (Figure 2.9). The filter cube, lens, and camera are mounted on a xyz-stage so that different regions of the chip can be focused on.

In order to image the behavior of particles or cells in the DLD array, we use GFP-fluorescent polymer microspheres in place of cells or GFP-fluorescently labelled cells. Fluorescent beads above the critical size of the DLD array being displaced from the outer sides of a DLD array toward the center in parallel DLD arrays are shown in Figure 2.10. The image was taken using the imaging setup described above and shown in Figure 2.9.
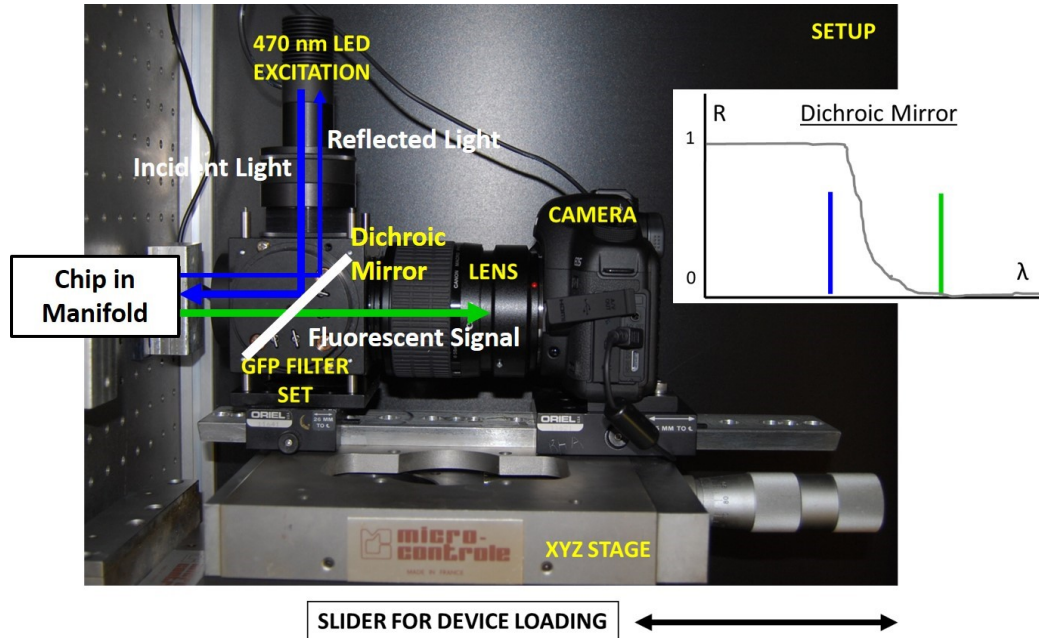
Figure 2.9: Imaging setup used to image fluorescent beads or fluorescently labeled cells traveling through the DLD array. Light from a blue LED (470 nm) is reflected off a dichroic mirror onto the chip. Green light from fluorescent particles that are excited by the blue incident light is emitted and passes through the dichroic mirror, through a lens, to the camera. Some of the blue incident light is reflected off the chip and off the dichroic back toward the light source.

2.5.2 Fluorescent Beads

Fluoresbrite YG microspheres (Polysciences, Inc.) with sizes of approximately 3 μm, 6 μm, and 10 μm were used to verify the critical sizes of the DLD arrays used in this thesis.

2.5.3 Leukocytes

Leukocytes are labelled with the green fluorescent nucleic acid stain, SYTO13. SYTO13 is added at concentrations of 6-10 μL per mL of whole blood. An incubation period of 45 minutes is observed after labelling before the experiment is run. The label becomes brighter with increasing incubation time up to at least 90 minutes, so regulation of the incubation time is important for experiments involving
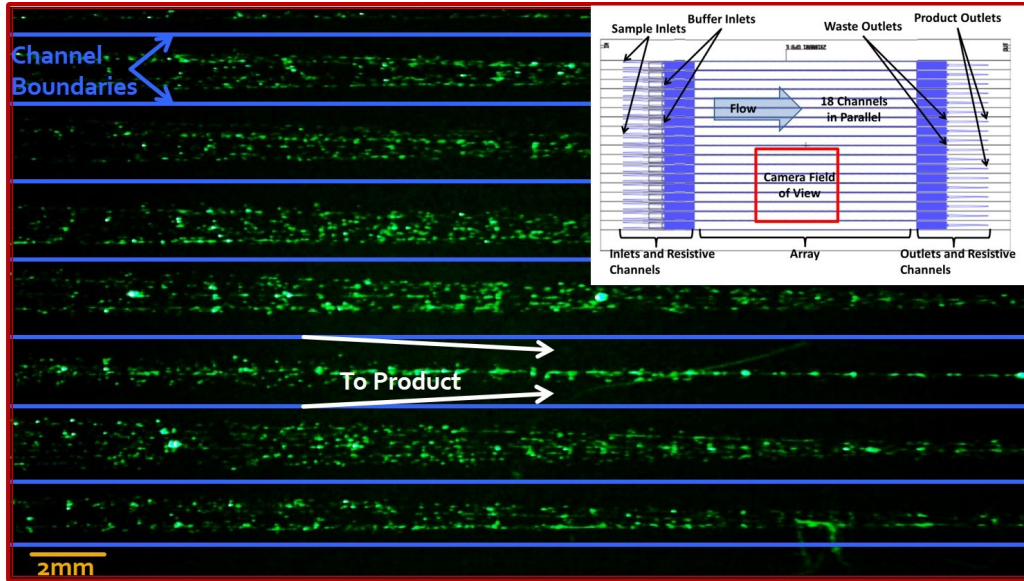
Figure 2.10: Image of 10 μm green fluorescent beads in 1.5 mm wide parallel DLD arrays with 18 μm circular posts, 18 μm gaps, and 1/42 tilt (critical size $\sim$4 μm). Adjacent DLD arrays are separated by horizontal blue lines in the image. Flow is from left to right, and the 10 μm beads, which are above the critical size of the DLD array, are directed from the outer sides of each DLD array toward the center.

measurement of the intensity of the fluorescence. No bleaching of SYTO13 from the blue LED in the imaging setup has been observed for time periods up to 90 minutes.

2.5.4 Cancer Cells

PC3 cancer cells that have been transfected with a green fluorescent protein (GFP) vector are used to enable imaging. The PC3 cancer cells were obtained from the lab of Dr. Ken Pienta at Johns Hopkins University School of Medicine.

2.6 Standard Blood Preparation and Disposal Protocols

Blood used in the experiments in this thesis is shipped overnight from Interstate Blood Bank (Memphis, TN), and experiments are performed within 36 hours of the time that the blood is drawn. All blood handling, including loading of the blood into the syringes, is performed in a Biosafety Level 2 (BSL-2) hood. Blood is diluted in a buffer containing anti-coagulants to prevent clot formation as discussed in Chapter 3 and filtered through a Steriflip 20 μm nylon net filter prior to loading into a syringe to remove any clots that may have formed during transit.

Disposal involves adding bleach to the blood to be disposed such that the final concentration is 10% bleach and disposing down the drain after 20 minutes have passed since the addition of the bleach. Syringes, tubing, hydrophobic filters, and barbed-luer fittings are disposed in a standard bio-hazard box. The manifold is disassembled and cleaned with ethanol. A 1% Contrad 70 solution can be used after this to remove any cells or other debris that remains on the manifold, and the manifold is soaked in a 1% Contrad 70 solution until next use.

Detailed information about ordering blood, preparing blood for experiments, and counting of cells in blood can be found in Appendix D.

Chapter 3

Inhibition of Clot Formation in DLD Arrays

3.1 Introduction

Previous work has focused on using DLD arrays to selectively capture rare cells of biological interest. D.W. Inglis et al. demonstrated that DLD arrays can be used to separate malignant lymphocytes from healthy lymphocytes [36]. L.R. Huang et al. have used DLD arrays to capture nucleated red blood cells from the peripheral blood of pregnant women for applications in prenatal diagnostics [32]. S.H. Holm et al. have used DLD arrays to separate parasites from human blood [26]. B. Zhang et al. have used DLD arrays to separate cardiomyocytes from blood [91]. Typical volumes of blood processed for such applications have been limited to 100 μL per DLD array.

While the capture efficiencies achievable with DLD arrays are sufficiently high to be useful in rare cell capture (>85%), capturing biologically useful quantities of rare cells requires processing of large volumes of blood. Recently, K. Loutherback et al. operated DLD arrays at flow rates as high as 10 mL/min, removing one key barrier to processing large volumes of blood [50]. However, even at this high flow rate, the

29

volume of blood processed was limited to less than 200 μL per DLD array due to clogging in the array. In this chapter, we demonstrate that this clogging process is due to the formation of blood clots and identify and inhibit the underlying physical and biological mechanisms driving this process.

Clot formation in DLD arrays imposes three significant limitations on device performance. First, the clot increases the fluidic resistance of the array, limiting the flow rate for a given pressure. Second, the clot formation can alter the flow pattern in a way that affects the critical size or simply displace cells below the critical size, making it appear that these cells behave similar to cells above the critical size and thus decreasing the enrichment. Third, the clot formation captures target cells, thus decreasing the yield of a separation process.

The limitations imposed by clot formation in the DLD array have been addressed in recent work. S. Zheng et al. showed that clogging occurred where the cells entered the array and explore the effects of dilution and age of the blood on clogging [93]. S.H. Holm et al. reported no clot formation with coagulation of blood being prevented by EDTA at a concentration of 6 mM. However, the volumes of blood being processed were still very small ($\sim$10 μL), the dilution was high (20x), and the flow rate was low ($\sim$3 μL/min) [26]. D.W. Inglis et al. mentioned the regular observation of blockages arising in the array from large clot-like structures in the blood despite the removal of such clot-like structures via pre-filtration before blood is loaded onto the array [37].

The effect of surface properties on clot formation in silicon microfluidic devices has been studied extensively [81]. Clot formation in DLD arrays has been observed in both silicon devices and PDMS devices, suggesting that activation of the contact activation coagulation pathway due to contact with silicon dioxide (glass) is not the dominant mechanism driving clot formation in DLD arrays [32, 93, 37]. In both silicon and PDMS DLD arrays, bovine serum albumin (BSA) has been used at a concentration of 1% (1g per 100 mL) to reduce non-specific adhesion [36, 32, 26, 91, 50, 37]. We

use BSA in this work at this concentration as a control in order to allow comparison with previous work.

Our experiments are conducted using DLD arrays reactively-etched in silicon to a depth of 160 μm by an anisotropic deep-etching process. The arrays are lidded with a pressure-sealing tape consisting of a thin silicone layer with a polyolefin backing. The lidded device is mounted in an acrylic manifold to which fluidic connections are made via O-rings. A dual-syringe pump is used to drive buffer and sample (diluted blood) through the chip. Flow velocities in the array are reported as the syringe volume flow rate divided by the cross section formed by the depth of the channel (160 μm) and the period of the array (post width + gap width = 100 μm) times the number of gaps through which the fluid is flowing (14 for a typical array) for a total effective width of 1.4 mm.

Whole adult human blood from healthy donors was purchased from Interstate Blood Bank (Memphis, TN) for use in our experiments. Blood samples were shipped overnight in acid citrate dextrose anti-coagulated tubes at a temperature of 4°C, and experiments were performed within 36 hours of the draw time. Blood was obtained, processed, and disposed of in accordance with policies and procedures set by the Princeton University Institutional Biosafety Committee (IBC) as described in Section 2.6 in the previous chapter.

3.2   Origins of Clot Formation

In order to capture rare cells in a product free from non-target cells present in blood, we use a three-input mirrored DLD array (Figure 3.1). Blood enters the chip through two through-holes (not shown) that each connect to four injector channels (visible via fluorescently tagged leukocytes) that lead to the top and bottom sides of the array. Buffer enters the chip through a through-hole (visible due to light from back of chip)
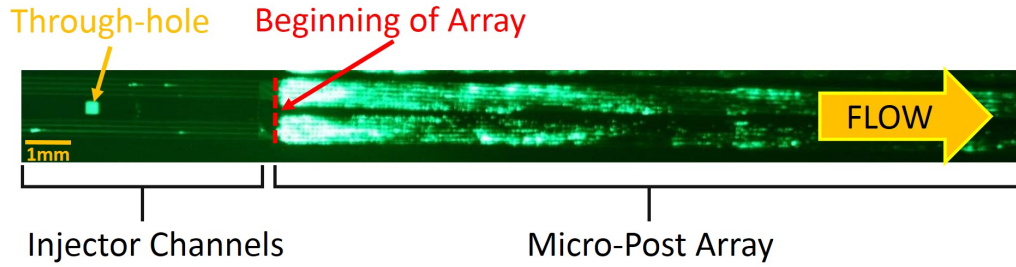
Figure 3.1: Fluorescent image of stained leukocytes in whole blood entering the DLD micro-post array through injector channels. Leukocytes are stained with SYTO13 at a concentration of 10 μL per mL of whole blood. Blood is diluted 1:3 in a running buffer composed of PBS, 1% BSA (1% = 1g per 100 mL), and 1 mM EDTA. The DLD array is a mirrored design in which sample enters at the outer sides of the array through four 40-μm-wide injector channels each on top and bottom, and cells larger than the critical size are displaced toward the center of the array, in which buffer alone is input through four 40-μm-wide injector channels. The array parameters are 60 μm right isosceles triangles, 40 μm gaps, and 1/50 tilt angle, yielding a critical size of approximately 6 μm. The array is 40 mm long, and each half of the mirrored array is 0.7 mm wide. The diluted blood input flow rate (total over both the top and bottom halves of the mirrored array) is 0.10 mL/min and the buffer input flow rate is 0.16 mL/min, giving a flow velocity of 1.8 cm/s. This image was taken with an exposure time of 2.5 seconds at t=30 minutes, after 0.7 mL equivalent volume of undiluted whole blood (2.8 mL of diluted blood in running buffer) had flowed through the array.

that leads to four injector channels (not visible, but which connects the through-hole to the beginning of the array) that lead to the middle of the array. There is a large amount of stuck fluorescent leukocytes at the beginning of the array. Experimentally, this is indicative of a clogging phenomenon that will cause an increase in the pressure for a given flow rate.

From the image in Figure 3.1 alone, we do not know if capture of the leukocytes at this location is caused by their direct adhesion to the posts or if they are caught due to clogging caused by a different mechanism. Further, note that the clogging does not occur in the injector channels and only happens at the beginning of the array. Since the injector channels are the same width as the gap in the micro-post array,

this is significant because it demonstrates that clogging happens dynamically at the beginning of the array and is not due to large clumps that have formed off-chip.
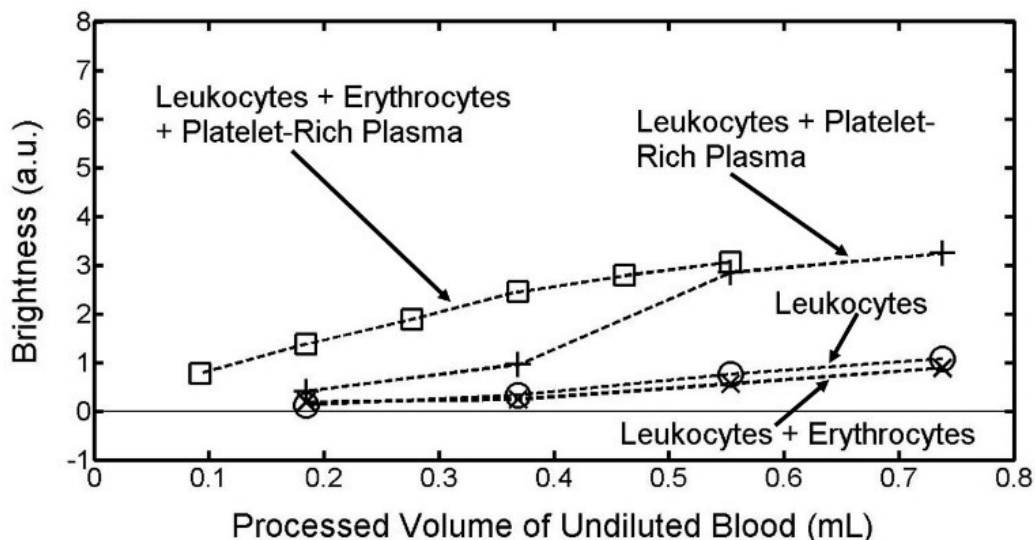
Figure 3.2: Fluorescent brightness of stuck leukocytes (integrated over the array) as a function of volume of components of blood processed corresponding to the volume of undiluted blood from which the components were obtained. Leukocytes are stained with SYTO13 at a concentration of 10 μL per mL of whole blood. Blood is separated into three components leukocytes, erythrocytes, and platelet-rich plasma using a combination of erythrocyte lysis buffer and centrifuge. Leukocytes are obtained via centrifuge after blood is treated with erythrocyte lysis buffer. Erythrocytes and platelet-rich plasma are obtained via pipette after centrifuge. The components are then diluted in a running buffer composed of PBS, 1% BSA (1% = 1g per 100mL), and 1 mM EDTA to a final volume of four times the volume of undiluted blood from which the components were obtained. DLD array parameters and flow velocity are the same as in Figure 3.1.

Blood contains three main components: leukocytes, erythrocytes, and a platelet-rich plasma. By experimentally removing or adding these different blood components before the sample enters the chip, we determine the relative contributions of the different components of blood to clogging. Leukocytes, because of their role in wound healing, have some adhesive properties, so we first isolate leukocytes via erythrocyte lysis buffer and centrifuge and re-suspend in a volume of running buffer equal to four times the original volume of blood from which the leukocytes were obtained.

33

Using the isolated leukocytes as the input to the chip, we see the leukocytes alone do not result in significant clogging (Figure 3.2). Note that the x-axis in Figure 3.2 represents the corresponding volume of the original blood from which the leukocytes were obtained, not the input volume to the chip which was four times greater. We use such a metric throughout the paper so one can directly relate results to the clinically relevant amount of blood processed. A very approximate but experimentally useful number for comparison is that the pressure begins to increase for a brightness of stuck leukocytes corresponding to a value of 1 on the y-axis in Figure 2. While the pressure increase alone might not be a problem, we note that when it occurs, the fluid flow in parts of the array is no longer parallel to the walls due to local clogging, which detrimentally affects the bumping mechanism.

Since erythrocytes do not have biologically significant adhesive properties, we then obtain a combination of erythrocytes and leukocytes via centrifuge by removing platelet-rich plasma via pipette and then re-suspending the erythrocytes and leukocytes in a volume of running buffer equal to four times the original volume of blood from which the leukocytes and erythrocytes were obtained. Similarly, we see that the combination of erythrocytes and leukocytes do not contribute significantly to clogging. However, when we run a combination of leukocytes and platelet-rich plasma diluted 4x in running buffer relative to the original volume of blood from which these were obtained (without erythrocytes), we see a substantial increase in clogging. Following this, we run a combination of erythrocytes, leukocytes, and platelet-rich plasma diluted 4x in running buffer relative to the original volume of blood from which these were obtained, and we observe a slight further increase in clogging, which is consistent with platelets being able to adhere to not just other platelets and leukocytes but also erythrocytes. These results suggest a conventional clotting process driven by platelets is the primary cause of clogging in the DLD array.

The surface of our chips is a thin coating of silicon dioxide from the oxygen plasma treatment and from reaction with air. Since it is well-known that contact with hydrophilic silicon dioxide causes clot formation through contact-activation coagulation [2], we examine two methods of preventing this: direct inhibition of the contact activation coagulation pathway and surface coatings. We used corn trypsin inhibitor to break the coagulation cascade due to contact activation by the surface by preventing the conversion of coagulation factor XII into XIIa [2]. Our results show that a 3.5 μM concentration of corn trypsin inhibitor results in a 40% decrease in clot formation, but not enough to enable 10X higher throughputs. We also examined the effect of a fluorocarbon coating to reduce the hydrophilic nature of the surface. The coating increased angle of 112° compared to a contact angle of 4° for our control surface. However, we found that this results in a two-fold increase in clot formation. This is consistent with prior work that showed with a wettability gradient on polyethylene that platelets under shear conditions adhere more strongly to hydrophobic surfaces compared to hydrophilic surfaces [76]. In order to further examine the contribution of protein adsorption on the silicon dioxide surface to clot formation, we use Pluronic F108, which is a block copolymer consisting of ethylene oxide and propylene oxide, in the running buffer at a concentration of 2 mg/mL instead of BSA [46]. Pluronic F108 reduces clot formation by less than 10% compared with BSA, which is consistent with protein adsorption onto the silicon surface not playing a major role in clot formation. The combination of these three results lead us to conclude that it is not surface effects but rather biological mechanisms that are involved in clot formation in DLD arrays.

3.3 Clot Formation Mechanisms

Clot formation is a very extensive field, and the processes driving clot formation in vivo are well understood. However, clot formation in our devices occurs in a shear-
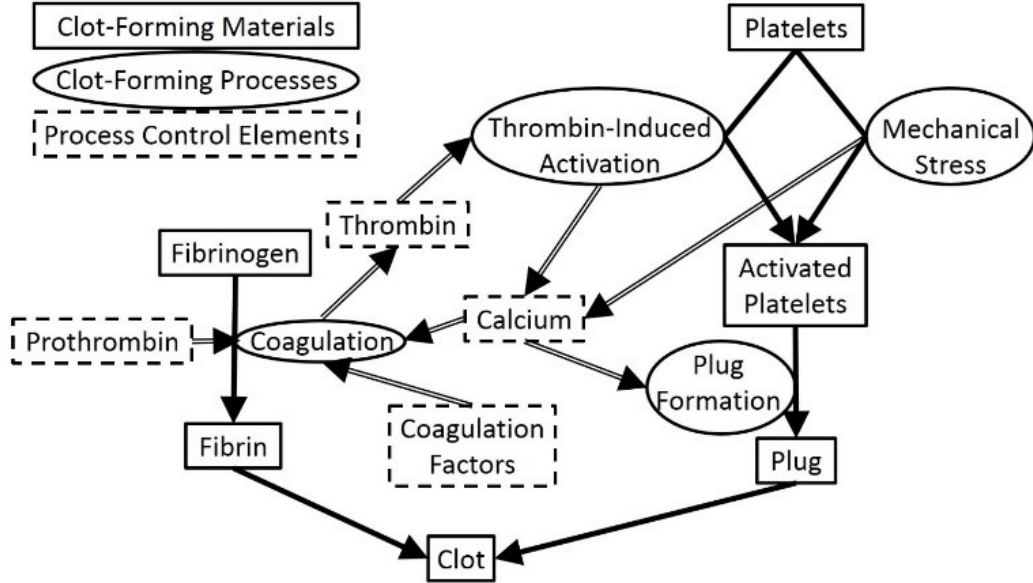
Figure 3.3: Simplified schematic diagram of conventional clot formation process involving both coagulation (left side) and platelet-activation (right side). Shown are the clot-forming materials (rectangles with solid borders), the mechanistic processes acting on these materials (dark arrows) and names of these processes (ovals adjacent to the dark arrows), and elements in blood that control these processes (rectangles with dashed borders). The light arrows show how the elements control the processes and which process create the elements. Note the feedback loop between the production of thrombin and the generation of calcium connecting the coagulation and platelet activation pathways. Adapted from [24].

dependent manner in a silicon device environment at shear rates higher than typical physiological levels ($>$1500 s^{-1}) and in a relatively short time ($<$1 s in the array). Thus, while the conventional understanding of clot formation in vivo may not be directly applicable, we use it as a framework to determine the mechanisms driving clot formation in DLD arrays.

Clot formation is driven by two complementary, mutually dependent processes shown schematically in Figure 3.3: platelet activation and coagulation. During platelet activation, the contents of stored granules are released into the blood plasma, triggering a clotting cascade, and the platelets change shape from spherical to stellate. Platelet activation can be triggered by a variety of factors, with thrombin-induced

platelet activation and mechanical stress-induced platelet activation being the two most relevant to DLD arrays. Coagulation involves the conversion of the soluble protein fibrinogen into insoluble strands of fibrin. In the coagulation cascade, prothrombin is converted into thrombin, which catalyzes the conversion of fibrinogen into fibrin in the presence of calcium to form a clot [24].

From this diagram, we notice two mutual positive feedback interactions between platelet activation and coagulation. First, thrombin, which is a product of the coagulation cascade, induces platelet activation by activating protease-activated receptors on the cell membrane of platelets [60]. Second, platelet activation causes the release of calcium ions into the blood plasma, which promotes coagulation. Therefore, both inhibiting the action of thrombin and chelating calcium ions should result in a significant reduction in clot formation due to the breaking of this feedback loop [24].

3.4   Reduction of Clogging

In this section, we examine the effectiveness of biochemical and physical methods for reducing clot formation in DLD arrays.

3.4.1   Chelation of Calcium and Inhibition of Thrombin

In order to inhibit the effect of calcium ions in the blood plasma, either ethylenediaminetetraacetic acid (EDTA) or acid citrate dextrose (ACD) can be used. While both work by chelating calcium, EDTA binds calcium more strongly and irreversibly than ACD. Recent studies have also found EDTA to be more effective than ACD at inhibiting the activity of the glycoprotein IIb/IIIa receptor, which is a key calcium-dependent integrin involved in platelet aggregation [11]. For these reasons, our work focuses primarily on EDTA. Our results (Figure 3.4) show that increasing the concentration of EDTA from 1 mM to 5 mM results in a 10-fold reduction in clot formation
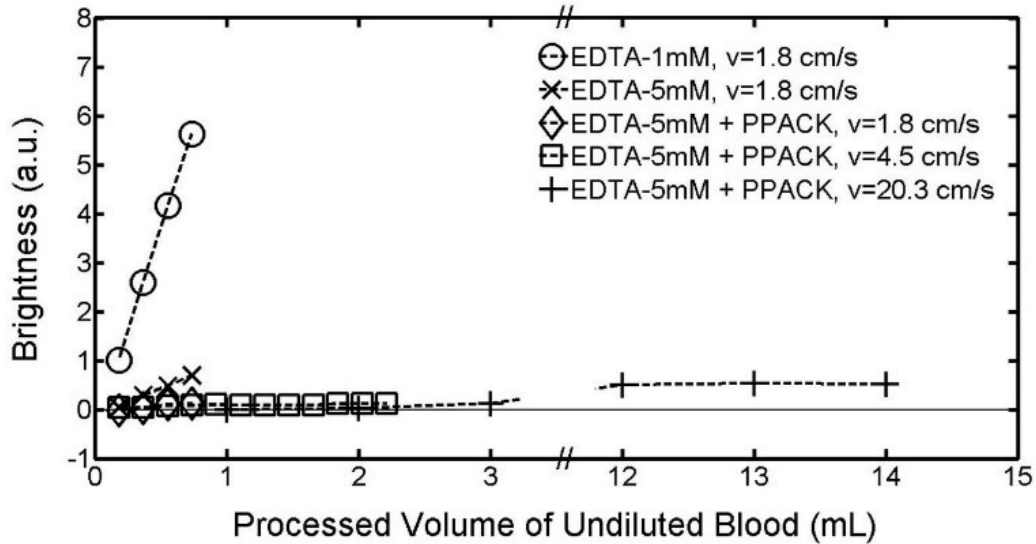
Figure 3.4: Effect of the calcium-chelating anticoagulant EDTA and the direct thrombin inhibitor PPACK on clot formation in the DLD array at flow velocities of 1.8 cm/s, 4.5 cm/s, and 20.3 cm/s. Clot formation is measured as the fluorescent brightness of stuck leukocytes as a function of the equivalent volume of undiluted whole blood that has passed through a single DLD array. Leukocytes are stained with SYTO13 at a concentration of 6 μL per mL of whole blood. Blood is diluted 1:3 in a running buffer composed of PBS, 1% BSA (1% = 1g per 100 mL), and either 1 mM or 5 mM EDTA. PPACK is then added so that the final concentration in the diluted blood is 40 μM. DLD array parameters are the same as in Figure 3.1.

as measured by the brightness of stuck leukocytes for up to ~0.7 mL equivalent volume of undiluted whole blood processed over a time of 30 minutes. While this is a significant reduction in clot formation, an even larger reduction is necessary to prevent an increase in pressure due to clot formation since pressure scales nonlinearly with the shrinkage of the gap caused by clot formation.

In order to inhibit thrombin-induced platelet activation, we use the direct thrombin inhibitor D-Phenylalanyl-L-prolyl-L-arginine chloromethyl ketone (PPACK). Compared to heparin, PPACK is more effective since it is able to act against both free thrombin and clot-bound thrombin, while heparin can only act against free thrombin [84]. We do not examine the effect of the direct thrombin inhibitor hirudin, as previous studies have found PPACK to be a similarly effective anticoagulant

for blood when used at a concentration of at least 40 μM [57]. Adding PPACK at a concentration of 40 μM on top of the 5 mM EDTA results in a further 5-fold reduction in clot formation (Figure 3.4). At a flow rate of 1.8 cm/s, after 30 minutes, during which time 0.7 mL of undiluted blood has been processed, only a barely discernible increase in stuck leukocytes due to clot formation is observed.
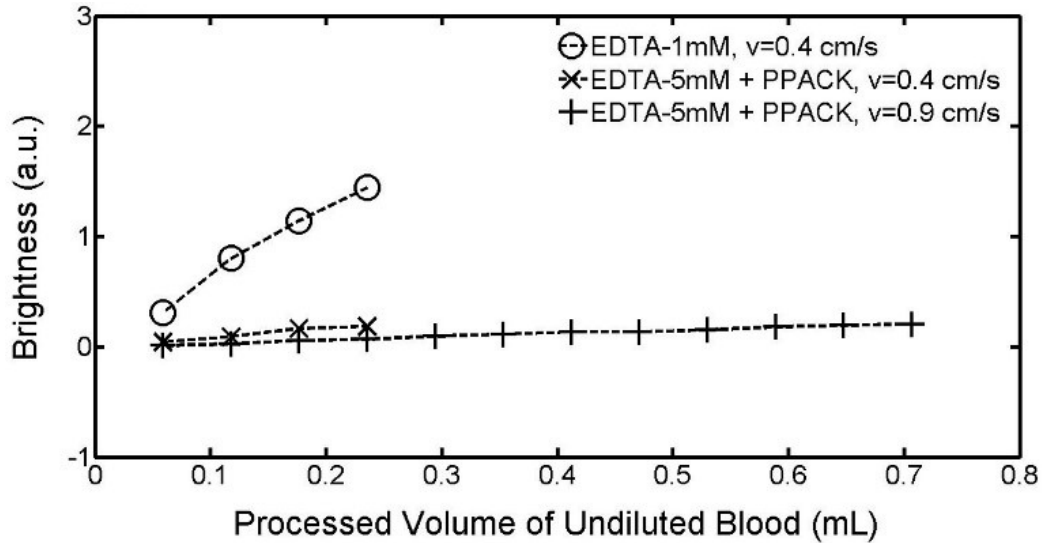

Figure 3.5: Effect of the calcium-chelating anticoagulant EDTA and the direct thrombin inhibitor PPACK on clot formation in a DLD array with circular posts at flow velocities of 0.4 cm/s and 0.9 cm/s. Except for DLD array parameters of 18 μm circular posts, 18 μm gaps, and 1/42 tilt angle, experimental conditions are as in Figure 3.4.

We also examined the effect of EDTA and PPACK on reducing clogging in arrays with circular posts. The results (Figure 3.5) were qualitatively similar. As with triangular posts, we observe a significant decrease in clot formation with the combination of 5 mM EDTA and 40 μM PPACK compared to the control of 1 mM EDTA.

In order to keep processing times under one hour even when processing large volumes of blood, we next examine the effect of flow rate on clot formation under conditions of optimal calcium chelation and thrombin inhibition described here.

3.4.2 Clot Formation, High Flow Velocity, and Processing Large Volumes of Blood

In addition to keeping processing times short even for large volumes of blood, there are two further reasons for increasing the flow velocity. First, increasing the flow velocity reduces the time in which platelets can form an aggregate within the array and reduces the time in which leukocytes can adhere to the micro-posts. Second, the higher shear stress from the higher flow velocity has been shown to cause disaggregation of platelet aggregates that have already formed [31]. On the other hand, a higher velocity gives a higher shear, which could cause more shear-induced platelet activation and clogging. Thus we performed experiments increasing the flow velocity first by a factor of 2.5 and then by a factor of 11.3 from the velocity of the previous section for triangular posts.

When we increase the flow velocity by a factor of 2.5 to 4.5 cm/s to achieve a higher processed volume in 30 minutes, we observe an additional two-fold reduction in clot formation over the first 0.7 mL and were able to successfully process 2.2 mL equivalent volume of undiluted whole blood over 35 minutes. We then increase the flow velocity to 20.3 cm/s to measure the extent of clot formation as 14 mL of blood flows through a single DLD array in 45 minutes. We again observe a similarly slow linear increase in the fluorescent brightness of stuck leukocytes over the entire 14 mL of blood (Figure 3.4).

At all three flow velocities, over the 30-45 minute experimental time, the stuck leukocytes do not appear primarily near the input end of the chip, but are rather uniformly distributed throughout the array. This leads us to conclude that no platelet-driven plug formation is observed with 5 mM EDTA and 40 μM PPACK, and that the slow linear increase in fluorescent brightness of stuck leukocytes is due to isolated leukocyte adhesion to the posts. Furthermore, the average shear rate at the flow velocity of 20.3 cm/s is 25,000 s^{-1}, which is more than 10 times typical physiological

shear rates of 50 s^{-1} to 2000 s^{-1} [20] and well above the 10,000 s^{-1} at which shear-induced platelet activation has been reported [27]. Even under these conditions, the combination of 5 mM EDTA and 40 μM PPACK prevents platelet plug formation in DLD arrays. We note that the high shear may also have a positive benefit of detaching adherent cells from the posts [53]. High flow rates were also tested with circular posts (Figure 3.5), and again large volumes could be processed with minimal clogging.

3.4.3 Effects of Mechanical Stress and Gap Scaling on Clot Formation

We seek the source which initiates the clogging process in the array. Mechanical stress, particularly in the form of shear stress in a microfluidic channel, is a well-known cause of platelet activation, which could lead to clot formation [69, 27, 25]. From Figure 3.1 and similar experiments, we do not observe any clogging in the injector channels leading to the array. This implies that shear at sidewall alone is not a major source of clogging. Figure 3.6 shows a 2-D simulation of the flow speeds in the injector channels and DLD array with triangular posts. For 150 μm depth channels, the simulation condition represents a flow of 110 μL/min per injector channel, which is comparable to an input flow rate of 1.30 mL/min for the chip of Figure 3.1. Shear stresses in the injector channels have a peak of 16,000 s^{-1}, which is comparable to the peak shear stress in the gap in the array. However, experimentally, even at shear rates exceeding this, only negligible clogging is observed in the injector channels.

As seen in Figure 3.1, the clogging begins at the start of the DLD array. From the simulations, the peak shear stress in the injector channels does not differ significantly from the peak shear stress in the array, but the shear stress increases and decreases rapidly vs. time as the fluid accelerates and decelerates in the array. It has previously been shown that for a single constriction, similar to a single gap in the array, in a
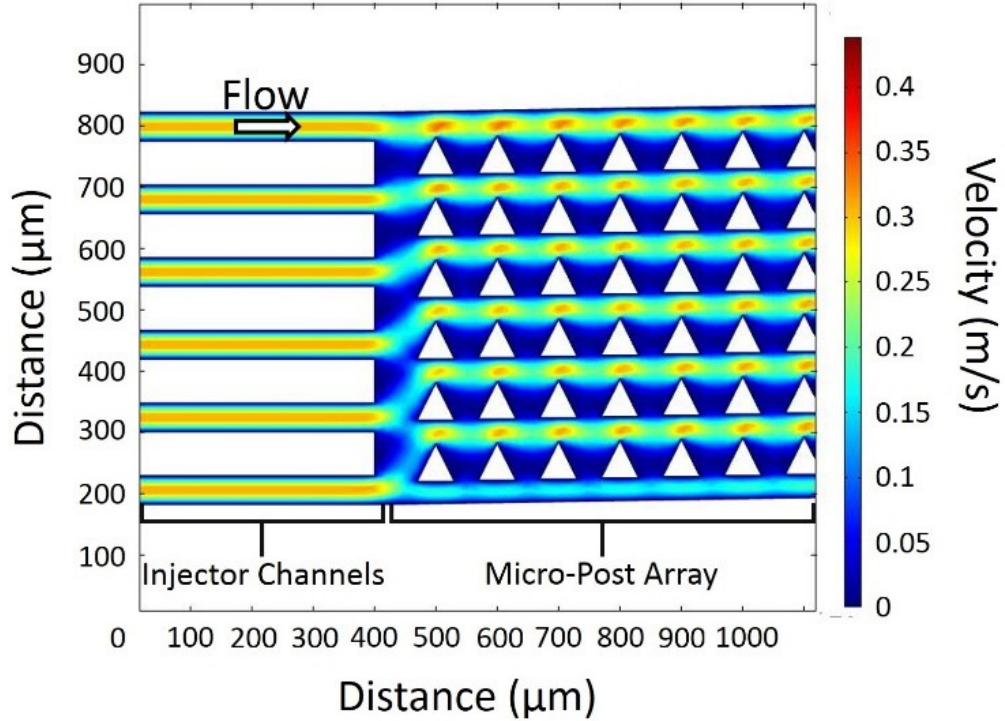
Figure 3.6: Color contour plot of the magnitude of the flow velocity in the injector channels and beginning of the DLD micro-post array. The injector channels are 40 μm wide, and the micro-post array is composed of 60 μm right isosceles triangles with 40 μm gaps and a 1/50 tilt. Note that the magnitude of the velocity is constant in the injector channels whereas there is acceleration and deceleration in the micro-post array. The conditions in this simulation correspond to an average flow velocity of 11 cm/s as described in Figure 3.1.

blood vessel, a clot expands from a small aggregate of platelets through adhesion of platelets in the low-shear zones at the downstream face of the clot [59]. While no such low-shear zones exist in the injector channels, the acceleration and deceleration of the fluid in the gaps provide a number of such low-shear zones for a clot to form.

Shear-induced platelet activation requires platelet membrane glycoproteins Ib and IIb-IIIa as well as the presence of von Willebrand factor [63]. We measure the effect of the glycoprotein IIb-IIIa inhibitor tirofiban at a concentration of 100 ng/mL of blood to test the contribution of shear-induced platelet aggregation to clot formation [73]. Our results (with 1 mM EDTA) show that tirofiban at this concentration reduces clot

formation by 40% at a flow velocity of 1.8 cm/s for the first 0.7 mL of blood through the array. This provides further support that mechanical shear stress is an important factor in initiating the clogging process in the array.
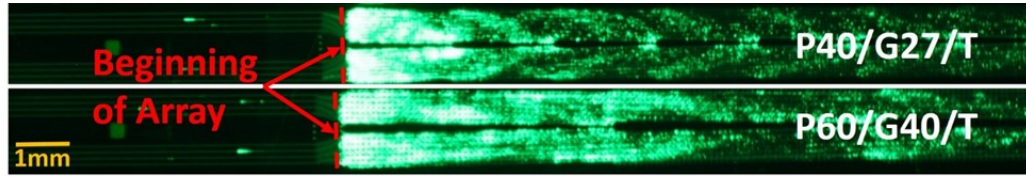

Figure 3.7: Fluorescent image of stained leukocytes in whole blood entering two DLD micro-post arrays (right of dashed red line) through injector channels (left of dashed red line). Leukocytes are stained with SYTO13 at a concentration of 10 μL per mL of whole blood. Blood is diluted 1:3 in a running buffer composed of PBS, 1% BSA (1% = 1g per 100 mL), and 1 mM EDTA. The DLD arrays are a mirrored design as in Figure 3.1. The array parameters are 40 μm right isosceles triangles, 27 μm gaps, and 1/28 tilt angle for the top DLD array and 60 μm right isosceles triangles, 40 μm gaps, and 1/50 tilt angle for the bottom DLD array. This image was taken with an exposure time of 2.5 seconds at t=30 minutes, after 0.4 mL equivalent volume of undiluted whole blood (1.6 mL of diluted blood in running buffer) had flowed through the top DLD array and 0.7 mL equivalent volume of undiluted whole blood (2.8 mL of diluted blood in running buffer) had flowed through the bottom DLD array.

We examined the effect of scaling the gap size by comparing the clogging in two triangular arrays − one with post and gap of 40 μm and 27 μm, respectively, and the second with post and gap of 60 μm and 40 μm, respectively, with only 1 mM EDTA added to the input mixture (Figure 3.7). A qualitatively different clogging pattern was observed as the gap was reduced; there was more clogging immediately after the beginning of the array (much more intense fluorescence), and less farther downstream. This qualitative difference was consistently observed over different flow speeds. In order for a larger gap to become clogged by a clot, an aggregate of platelets at least as large as the gap needs to form. Thus, for a given concentration of platelets, it takes longer for such an aggregate to form since it would require a greater number of platelet-platelet interactions. Furthermore, if the inlets are held at a fixed pressure, the flow velocity in the DLD array with the smaller gap will be slower than in the DLD

array with the larger gap, leading to more time for clots to form. Rapid clogging near the array inlet would prevent the transport of leukocytes (and platelets and other clotting agents) downstream to the farther end of the array. The combination of these effects explains the more rapid clogging right at the beginning of the array with smaller gaps.

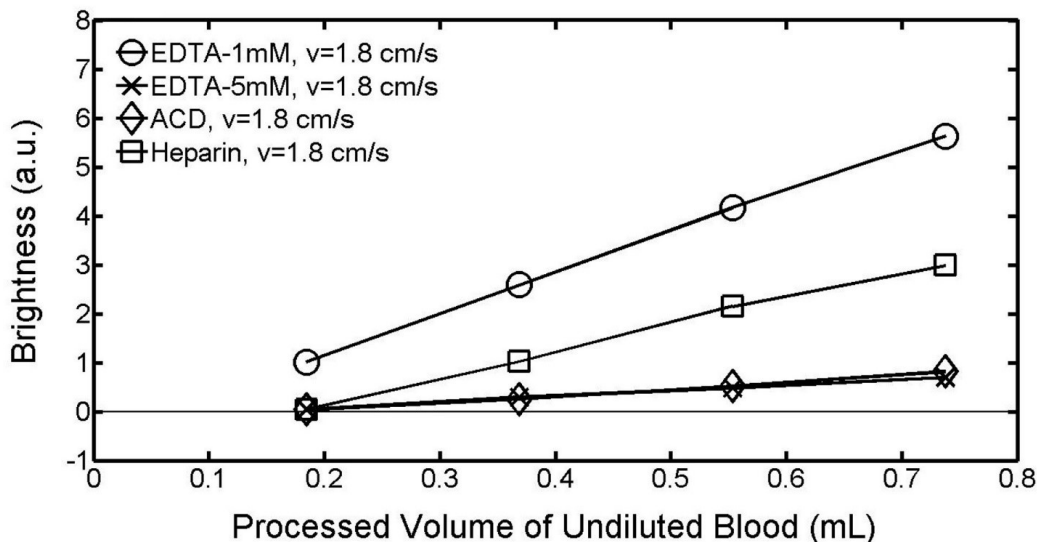### 3.4.4 Effects of Acid Citrate Dextrose and Heparin on Clot Formation

Figure 3.8: Effect of the calcium-chelating anticoagulants EDTA and ACD and the indirect thrombin inhibitor heparin, on clot formation in the DLD array at a flow velocity of 1.8 cm/s. Clot formation is measured as the fluorescent brightness of stuck leukocytes as a function of the equivalent volume of undiluted whole blood that has passed through a single DLD array. Leukocytes are stained with SYTO13 at a concentration of 6 μL per mL of whole blood. Blood is diluted 1:3 in a running buffer composed of PBS, 1% BSA (1% = 1g per 100 mL), and either 1 mM EDTA, 5 mM EDTA, 1:9 diluted ACD, or 40 units/mL heparin. DLD array parameters are the same as in Figure 3.1.

We examine the effect of two other commonly used anticoagulants, acid citrate dextrose (ACD) and heparin, on clot formation in DLD arrays. Like EDTA, ACD also inhibits clot formation by chelating free calcium ions, although less strongly and irre-

versibly than EDTA. Similar to PPACK, heparin inhibits clot formation through inhibition of thrombin, although the inhibitory mechanism of heparin is indirect through the activation of the enzyme inhibitor antithrombin III rather than directly inhibiting the active site of thrombin as PPACK does.

ACD binds calcium less strongly and irreversibly than EDTA. We use the standard ACD solution A, which is composed of 22.0 g/L C3434 (Citric Acid, trisodium salt, dihydrate); 7.3 g/L C0759 (Citric Acid, anhydrous); and 24.5 g/L G7528 (D-(+)-Glucose), added to the buffer at the recommended dilution ratio of 1:9. The difference in clot formation as observed from the fluorescent brightness of stuck leukocytes between 1:9 ACD and 5 mM EDTA is very small (Figure 3.8), further demonstrating the importance of calcium ions in the clot formation process in DLD arrays.

Heparin activates the enzyme inhibitor antithrombin III, which inactivates thrombin and other proteases involved in clot formation. We add heparin sodium salt to the buffer such that the final concentration of heparin is 40 units/mL. There is significantly more clot formation as observed from the fluorescent brightness of stuck leukocytes with heparin than with either 5 mM EDTA or 1:9 ACD (Figure 3.8). This is consistent with previous work by J.I. Weitz et al. showing that clot-bound thrombin (thrombin bound to fibrin) is not inhibited by heparin but is inhibited by PPACK and hirugen, which is another synthetic direct thrombin inhibitor [85].

3.4.5 Effects of Anti-Platelet Drugs on Clot Formation

Anti-platelet drugs are used to inhibit clot formation by preventing platelet aggregation. Tirofiban, which we discuss in Section 3.4.3 above, is one such drug that works by inhibiting platelet membrane glycoproteins IIb-IIIa, which are involved in shear-induced platelet aggregation. Recently, combinations of anti-platelet drugs have been used to improve effectiveness of platelet aggregation inhibition through synergistic effects between different anti-platelet drugs.
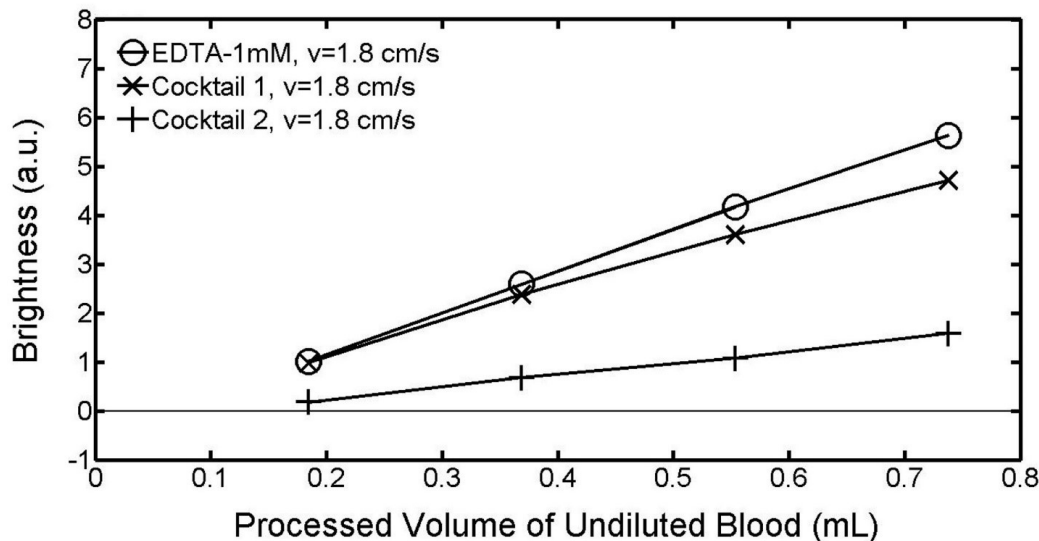
Figure 3.9: Effect of anti-platelet drug cocktails on clot formation in the DLD array at a flow velocity of 1.8 cm/s. Clot formation is measured as the fluorescent brightness of stuck leukocytes as a function of the equivalent volume of undiluted whole blood that has passed through a single DLD array. Leukocytes are stained with SYTO13 at a concentration of 6 μL per mL of whole blood. Blood is diluted 1:3 in a running buffer composed of PBS, 1% BSA (1% = 1g per 100 mL), and 1 mM EDTA. In addition, Cocktail 1 contains 100 μM aspirin, 10 μM clopidogrel, and 100 μM dipyridamole, and Cocktail 2 contains the same as Cocktail 1 plus 30 μM cilostazol. DLD array parameters are the same as in Figure 3.1.

One particularly powerful combination of anti-platelet drugs that has been examined recently is the combination of aspirin, clopidogrel, and dipyridamole [28]. We add these drugs to the diluted blood sample such that the final concentrations are 100 μM aspirin, 10 μM clopidogrel, and 100 μM dipyridamole. The decrease in clot formation is a modest 15% over the first 0.7 mL of blood through the DLD array (Cocktail 1, Figure 3.9). The inhibition of shear-induced platelet aggregation by another anti-platelet drug, cilostazol, has been shown to be enhanced by the presence of dipyridamole [29]. We run the experiment with the four anti-platelet drugs added to the diluted blood sample such that the final concentrations are 100 μM aspirin, 10 μM clopidogrel, 100 μM dipyridamole, and 30 μM cilostazol. The decrease in clot

formation is 75% over the first 0.7 mL of blood through the DLD array (Cocktail 2, Figure 3.9), which is a significant improvement from the addition of 30 μM cilostazol.

Even the powerful anti-platelet drug cocktails we examine here are significantly less effective in inhibiting clot formation in DLD arrays than the combination of EDTA and PPACK we describe in Section 3.4.1. Furthermore, the cost of inhibiting clot formation in DLD arrays with the anti-platelet drug cocktails we describe here is approximately ten times higher per unit volume of blood compared with the method using EDTA and PPACK we describe in Section 3.4.1. Thus, inhibition of clot formation in DLD arrays via calcium chelation (EDTA) and direct thrombin inhibition (PPACK) is both the most effective and the most cost effective.

3.4.6 Effects of Flow Rate and Blood Dilution on Clot Formation

While chemical and biological factors affect the affinity of platelets towards aggregation, the actual formation of a clot is a physical process affected by physical factors. Interactions between platelets are necessary in order for platelet aggregates to form, and the interaction frequency is determined by the concentration of platelets. A second factor that affects whether platelets form aggregates is the duration the platelets are in the chip. This is controlled by the flow velocity.

Under the control conditions of 1 mM EDTA in the buffer, we examine how these two factors affect clot formation in the DLD array (Figure 3.10). Assuming an interaction between two platelets is necessary for aggregation, increasing the dilution will reduce the interaction frequency by the square of the increase of the dilution. We observe that a 3.3-fold increase in the dilution and a corresponding 10-fold decrease in interaction frequency significantly slows the rate of clot formation for the same flow velocity.
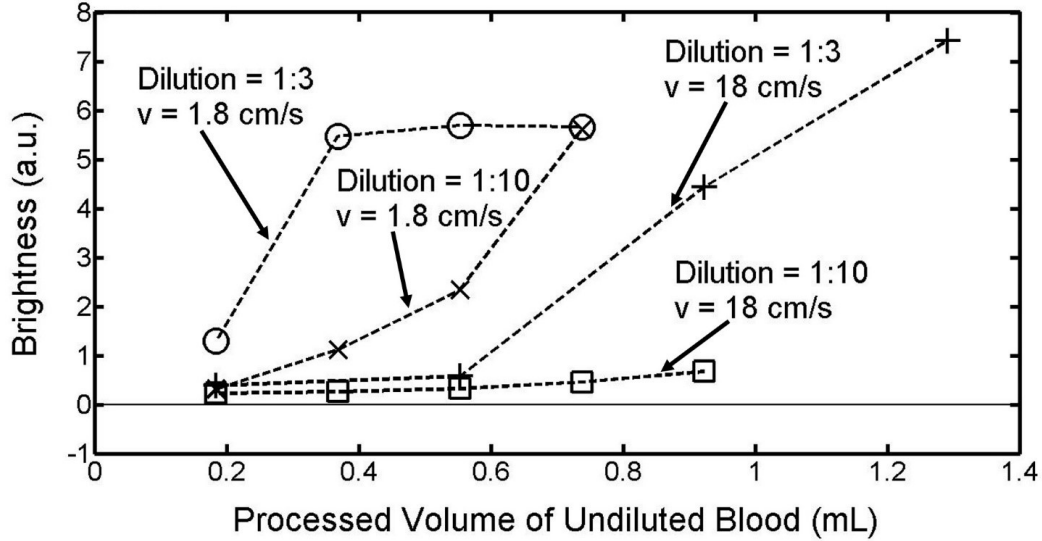
Figure 3.10: Effect of flow rate and blood dilution on clot formation in DLD arrays. Clot formation is measured as fluorescent brightness of stuck leukocytes as a function of the equivalent volume of undiluted whole blood that has passed through a single DLD array. Leukocytes are stained with SYTO13 at a concentration of 10 μL per mL of whole blood. Blood is diluted either 1:3 or 1:10 in a running buffer composed of PBS, 1% BSA (1% = 1g per 100 mL), and 1 mM EDTA. DLD array parameters are 60 μm right isosceles triangles, 40 μm gap, and 1/50 tilt angle, and the flow velocities used are either 1.8 cm/s or 18 cm/s.

Increasing the flow velocity by a factor of 10 reduces the time in which platelets can form an aggregate within the array by a factor of 10. The higher flow velocity also has the added benefit that higher shear stress has been shown to cause disaggregation of platelet aggregates that have already formed [31]. We observe that this 10-fold reduction in the time for aggregation formation significantly slows that rate of clot formation. Combining the 10-fold decrease in collision efficiency with the 10-fold decrease in aggregate formation time, we show that clot formation can be reduced by a factor of 10 as measured by the fluorescent brightness of stuck leukocytes.

3.5 DLD Array Performance for High Volume Separation at High Flow Rates

Table 3.1: DLD Array Performance for High Volume Separation at High Flow Rates for Different Array Parameters

	PC3 Cancer Cells	Leukocytes	Erythrocytes
Post: 60μm, Gap: 40μm, Tilt: 1/50, Triangular Posts, Center Wall Sample Input Volume: 56 mL	Sample: 3.1×10^4/mL Product: 8.2×10^4/mL Sample/Product Volume: 3.4 Yield: 77%	Sample: 1.7×10^6/mL Product: 5.0×10^5/mL Sample/Product Volume: 3.4 Yield: 8.6%	Sample: 1.2×10^9/mL Product: 1.8×10^8/mL Sample/Product Volume: 3.4 Yield: 4.5%
Post: 64μm, Gap: 34μm, Tilt: 1/26, Circular Posts, No Center Wall Sample Input Volume: 56 mL	Sample: 3.2×10^4/mL Product: 8.0×10^4/mL Sample/Product Volume: 2.9 Yield: 86%	Sample: 1.9×10^6/mL Product: 7.1×10^4/mL Sample/Product Volume: 2.9 Yield: 1.3%	Sample: 1.3×10^9/mL Product: 1.1×10^6/mL Sample/Product Volume: 2.9 Yield: 0.03%

We then tested the performance of three-input mirrored DLD arrays, as in Figure 3.1, to harvest prostate cancer cells (PC3) from blood using the conditions for minimum clogging from Section 3.4.1. The fractions of the total number of cancer cells, leukocytes, and erythrocytes, respectively that appear in the product compared to that processed through the input are measured to characterize the device performance. The fraction of cancer cells, the diameters of which are above the critical size of the array, is taken as a measure of the collection efficiency. The fraction of undesired erythrocytes (RBCs) appearing in the product is a measure of the depletion efficiency, which is another important parameter in characterizing three-input mirrored DLD arrays (a low yield is desired). The fraction of leukocytes (WBCs) appearing in the product is also measured so that the enrichment of cancer cells and purity of the product can be calculated. The target PC3 prostate cancer cells have an average diameter of 17 μm [52]. The results of our experiments are summarized in Table 3.1.

As a first experiment, the PC3 cells are collected along a central wall in the middle of the array with triangular posts, as in Figure 3.1 [34]. With array parameters of 60

μm triangular posts, 40 μm gaps, and 1/50 tilt angle, the critical size is approximately 6.1 μm. The array length was 40.00 mm, the total width of the array region including the center wall was 1.44 mm, with 0.62 mm width of post array in both the top half and bottom half of the array. The product is collected from a region spanning the central 0.22 mm of the array including the center wall. GFP-labelled PC3 cells were spiked in 14 mL of whole blood diluted 1:3 in a running buffer composed of PBS, 1% BSA, 5 mM EDTA, and 40 μM PPACK at an approximate concentration of $3x10^4$ per mL. After running through the array for 45 minutes at a flow velocity of 20.3 cm/s (processing an input volume of 56 mL), the collection efficiency of PC3 cells into the product outlet was 77%. However, erythrocyte contamination of the product was significant with nearly 4.5% of the input erythrocytes appearing in the product. At the high Reynolds number used in these flows (Re $\sim$ 10), it has recently been reported that erythrocytes, which have a discoid shape, behave in a DLD array as if they have a much larger size than they do at low Reynolds number, an effect not observed for circular posts [70]. Thus more are collected as large cells than would otherwise occur.

We then created an array with 64 μm circular posts, 34 μm gaps, and 1/26 tilt angle, for which the critical size is approximately 10 μm. The central collection wall in the mirrored array was also removed to present fewer surface for leukocyte sticking − the fluidic balance between the top and bottom regions kept the output buffer stream confined to this central region [34]. The array length was 38.22 mm, the total width of the array region including the central collection region was 2.24 mm, with 1.06 mm width of post array in both the top half and bottom half of the array. The product is collected from a region spanning the central 0.35 mm of the array including the collection region. The experiment is run under the same conditions as the first experiment except that the duration is now 38 minutes and the average flow velocity is 21.7 cm/s. The collection efficiency of PC3 cells is 86%, slightly higher than in

the triangle post chip, but the erythrocyte yield has dropped over 100X, from 4.5% to 0.03%, and now consists of small clumps of 3-5 erythrocytes. This surprising very large effect of the post shape on undesired erythrocyte collection will be one of the main topics of Chapter 4.

This represents the highest collection efficiency of cancer cells for a large volume of diluted whole blood (>7.5 mL) processed in a short time (<1 hour). By comparison, E. Sollier et al. used size-selective vortex technology to process 7.5 mL of blood in 20 minutes but achieved a maximum collection efficiency of less than 10% [74]. Using another inertial cell separation technique, slanted spiral microfluidics, M.E. Warkiani et al. processed 7.5 mL of blood in 8 minutes achieving a capture efficiency greater than 80%, but use of this technology requires lysis of red blood cells before processing [83].

3.6   Conclusions

Clogging in DLD arrays processing blood has limited their applicability for capture of rare cells to blood volumes well under 1 mL for each array. In this chapter, we have first shown that clogging of the array is caused by a conventional platelet-driven clot formation process. Next, we identified the presence of calcium ions and thrombin as drivers of platelet-driven clot formation process and disabled these two drivers using the calcium-chelating anticoagulant EDTA and the direct thrombin inhibitor PPACK.

Using these approaches, we have demonstrated that 14 mL of blood can be processed using a single DLD array in less than 45 minutes at flow velocities as high as 20 cm/s with no significant clot formation by the successful harvesting of PC3 prostate cancer cells from blood. Future work could include using a second DLD array in series to further concentrate the harvested cells [30]. Standard micro-fabrication techniques

have been previously used to produce a chip containing 15 DLD arrays in parallel, which would require an area of 36 mm by 70 mm for the array presented in this paper [91, 40]. Combining a chip containing 15 of our DLD arrays in parallel with the advances presented in this chapter should allow for processing of well over 100 mL of blood for rare cell capture in less than one hour.

The work in this chapter was largely described in [18].

Chapter 4

Post Geometry Design for High-Throughput Harvesting of Nucleated Cells from Blood with Minimal Erythrocyte Contamination Using DLD Arrays

4.1 Introduction

Separation of rare cells from whole blood using DLD arrays requires processing large volumes of blood in short times. In the previous chapter, we demonstrated an approach to inhibit clot formation in DLD arrays, allowing for separation of PC3 cancer cells from 14 mL of blood in less than one hour using a single DLD array [18]. In this chapter, we examine how post geometry affects capture efficiency of target cells above the critical size of the array and rejection efficiency of cells below the critical size of the array, specifically at high flow rates corresponding to Re>1.

As the flow rate increases, the shear the cells experience passing through the gap between the micro-posts increases, resulting in compression of the cells against the micro-posts. This compression can be sufficient to reduce the size of these cells below the critical size of the array, causing these cells not to be displaced. Z. Liu et al. have shown that significantly greater compression of cancer cells occurs with circular posts than with asymmetric triangular posts, resulting in a 4-fold decrease in capture efficiency at mL/min flow rates for the same array critical size [47]. However, in the previous chapter, we also demonstrated that erythrocyte contamination of the product increases significantly at high flow rates with asymmetric triangular posts, which should indicate that the erythrocytes effectively acted larger at higher flow rates, not smaller. Further puzzling is that this last effect does not occur with circular posts.

The mechanism that causes this increase in erythrocyte contamination of the product with asymmetric triangular posts but not circular posts at high flow rates, and correspondingly higher (moderate) Re, has not been previously studied. As background, inertial effects in DLD arrays at moderate Re (5<Re<40) have been studied, with an observed increase in separation efficiency with increasing Re due to a decrease in critical size resulting from asymmetry of the array [54]. It has also been suggested that the increasing separation efficiency results partly from shear-gradient lift forces arising from vortices that form behind the micro-posts at 5<Re<40 [56]. The behavior of erythrocytes in DLD arrays has also been examined, since the shape of erythrocytes is discoid and not spherical. J. Beech et al. showed that channel depth can be used to change the orientation of the erythrocytes such that the erythrocyte behaves as a spherical particle with size corresponding to either the long or short axis of the discoid [4]. More recently, post geometry was used to induce changes in the orientation (flipping) of the erythrocytes to achieve a similar effect in DLD arrays

with deep channels, in which the erythrocytes would normally be expected to behave as spherical particles with size corresponding to the short axis of the discoid [88, 70].

We begin in Section 4.2 with an overview of the fundamental mechanisms that govern particle (cell) behavior in microfluidic devices at high flow rates (moderate Re). In Section 4.3, we explain the experimental structures and modelling of streamlines. We then experimentally determine and fundamentally explain (i) (Section 4.4) how post geometry affects cell compression due to shear resulting in reduced yield of leukocytes and (ii) (Section 4.5) undesired erythrocyte displacement at high flow rates. Finally, in Section 4.6, we show that with optimal post shape, high yield (∼85%) of leukocytes with efficient rejection of erythrocytes (>99.98%) can be achieved at up to Re of 2.3, corresponding to processing of nearly 4mL of blood in less than 45 minutes in a single mirrored DLD array.

4.2 Fundamental Mechanisms at High Flow Rates

At these high flow rates, corresponding to Re of ∼15, we have found that the capture efficiencies of the large cells above the critical size of the array can degrade and the rejection of the small cells below the critical size of the array decreases. In this chapter, we examine the fundamentals behind this performance degradation and show how both can be affected by post shape. With optimal post shape, high yield of leukocytes (∼85%) with efficient rejection of erythrocytes (>99.98%) can be achieved up to Re of 2.3, corresponding to processing of nearly 4mL of blood in less than 45 minutes.

4.2.1   Changes in Fluid Flow at High Re

As Re increases, terms that could be neglected in the Navier-Stokes equation at low Re become significant. Assuming no external body forces, the full Navier-Stokes equation is:

$$\rho \cdot (\frac{\partial \mathbf{u}}{\partial t} + (\mathbf{u} \cdot \nabla)\mathbf{u}) = -\nabla P + \mu \nabla^2 \mathbf{u} \qquad (4.1)$$

where ρ is the density of the fluid, $\mathbf{u}$ is the fluid velocity, P is the pressure, and μ is the dynamic viscosity of the fluid. At low Re, the inertia terms, which are the two terms on the left-hand side of equation 4.1, are neglected. These terms are called "inertial" because they depend on changing the momentum (or the "inertia") of the particle. Note that these terms depend on the mass density times the the velocity or the time derivative of the velocity. The first term is always neglected in analysis of DLD arrays, since we do not consider the time-evolution of the flow; we only consider steady-state. The second term results from considering the transport of the velocity field in the flow (material derivative of the velocity). As we increase Re, this term becomes increasingly significant, because it is proportional to the square of the velocity, leading to the effects we consider below.

The Reynolds number, Re, in the DLD array is defined as

$$Re = \frac{\rho u G}{\mu} \qquad (4.2)$$

where ρ is the density of water at room temperature, u is the average velocity of the fluid in the gap, G is the width of the gap between the posts, and μ is the dynamic viscosity of water at room temperature. A particle Reynolds number, Re_p, has also been used to characterize hydrodynamic lift forces and can be calculated from the DLD array Re in equation 4.2 as:

$$Re_p = Re\frac{a^2}{G^2} \tag{4.3}$$

where a is the radius of the particle [77]. Re_p is less than 1 for all experiments and models in this chapter, and we state all results in terms of the DLD array Re.

It has previously been shown using rigid, non-deformable particles (polyethylene beads) that the critical size decreases by about 10% for circular posts as Re increases from 1 to 30 [56, 54]. At high Re, for particles that are denser than the fluid, such as erythrocytes and the polymer microsphere beads in our experiments, it has been shown previously that micro-post geometry becomes important due to the possibility of impaction of particles on the micro-posts as well as particles not following the streamlines due to rapid acceleration of the fluid around certain micro-post geometries [23, 3, 6].

We now examine inertial and shear effects in fluid flow and how these effects could affect the behavior of cells suspended in the fluid flowing through the DLD array at moderate Re (Re>1). The effects include inertial lift and Dean drag forces (Section 4.2.2), lift forces from hydrodynamic asymmetry (Section 4.2.3), centripetal acceleration effects (Section 4.2.4)and shear effects on cell shape (Section 4.2.5).

4.2.2   Inertial Lift and Dean's Flow Forces

In a straight micro-channel, suspended particles experience two oppositely directed lift forces as Re increases (Figure 4.1(a)). The shear-gradient lift force is directed from the center of the channel toward the walls and is a result of the parabolic flow profile. The wall effect lift force is directed away from the channel wall and decreases with distance from the wall. Both of these lift forces are caused by the effect the particle itself has on the fluid flow distribution. In a straight micro-channel, a minimum flow rate has been determined for the particles to reach stable equilibrium positions as
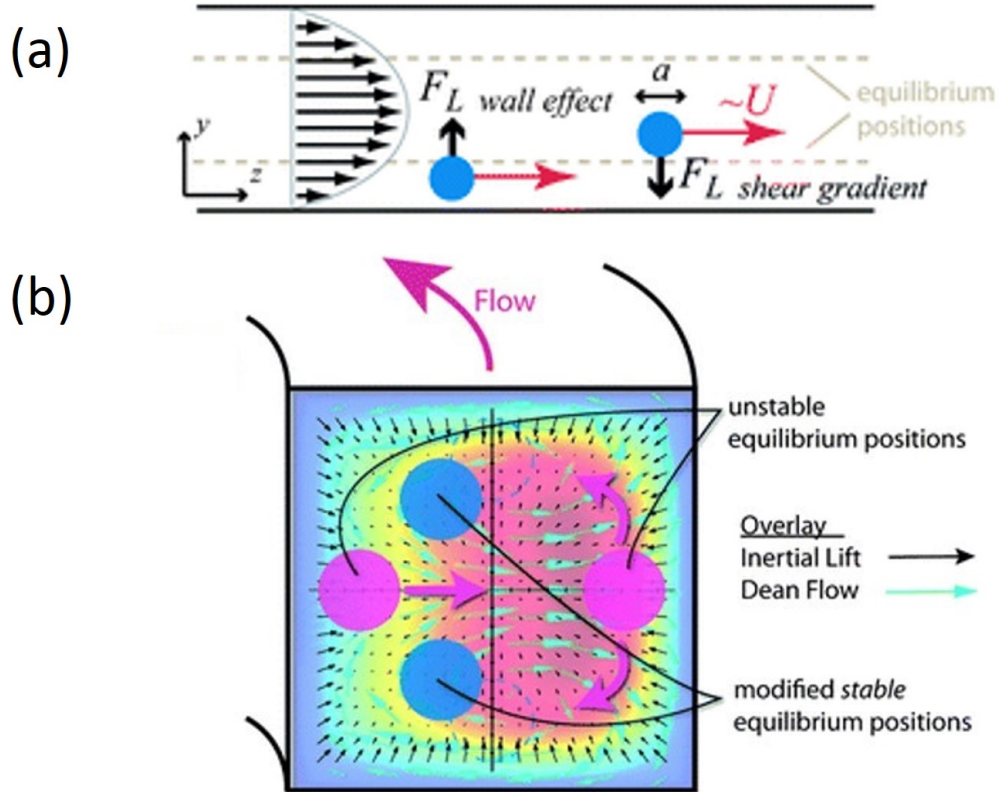
Figure 4.1: (a) Two oppositely directed inertial forces in straight micro-channels arise at high Re: a shear-gradient lift force directed away from the center of the channel and a wall-effect lift force that decreases with distance from the wall. Based on a balance between these two oppositely directed forces, particles can reach stable equilibrium positions. (b) In curved micro-channels, force from Dean's flow, which results from two counter-rotating vortices perpendicular to the flow direction, combines with the inertial lift forces to create stable and unstable equilibrium positions in the channel for particles suspended in the fluid. Image taken from [17].

a result of these two oppositely directed lift forces in a given length along the flow direction [17].

In curved micro-channels, Dean's flow is present in addition to these two lift forces. Dean's flow is caused by two counter-rotating vortices in the direction perpendicular to the flow, which result from the faster moving fluid near the channel center causing the more stagnant fluid near the walls to re-circulate in order to conserve mass (Figure 4.1(b)). These vortices result in a drag force on particles suspended in the fluid. The minimum flow rate for particles to reach equilibrium positions in this case is the

same condition as for the straight microchannel with an additional condition on the curvature of the channel relative to the channel width [17].

Theory to characterize the effect of inertial lift forces, specifically the shear gradient and wall lift forces, in DLD arrays has been developed and characterized by Lubbersen et al. [56]. Under the theory developed by Lubbersen et al., the flow rates we examine here are less than 0.01 the minimum flow rate required for particles to achieve stable equilibrium positions in the gap due to these inertial lift forces [56]. This makes it significantly less likely in our experiments that the shear-gradient and wall effect lift forces are causing particles below the critical size of the array to cross one or more streamlines and behave as particles above the critical size of the array compared to in the experiments of Lubbersen et al. [56], which were conducted at more than 0.2 times the minimum flow rate required for particles to achieve stable equilibrium positions due to these inertial lift forces. Note that the theory developed by Lubbersen et al. [56] is based on the length of the post in the direction of the flow, considering the channel length as the length of a single gap.

4.2.3   Lift Effects from Asymmetry

Less well-known than inertial (shear-gradient and wall effect) lift forces is the non-inertial hydrodynamic lift force for deformable particles, such as erythrocytes. Even in the regime of low Re, the symmetry of the Stokes regime (Re<1) can be broken in a way that enhances suspended deformable particles (vesicles) to undergo cross-streamline migration. This can occur due to asymmetry of the walls or interactions between suspended particles [19]. Non-inertial hydrodynamic lift has been used to separate circulating tumor cells from erythrocytes [21]. Hydrodynamic lift forces arising from asymmetry of the walls in this way have not been studied at Re above 1.
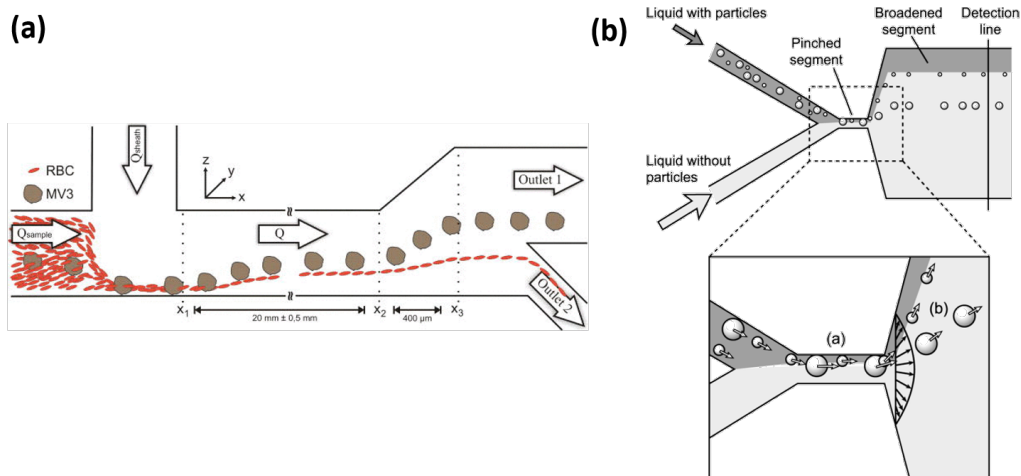
Figure 4.2: (a) Non-inertial hydrodynamic lift induced separation, which relies on asymmetry of the walls to enhance particles to cross streamlines, is used to separate MV3 melanoma cells from erythrocytes at Re of 0.37. Image taken from [21]. (b) Pinched flow fractionation, which relies on hydrodynamic effects resulting from liquid with particles and liquid without particles being injected into a pinched region that then expands into a wider region, is used to separate polymer microspheres of different sizes. For the geometry shown, separation is dependent upon the relative flow rates of the liquid with particles and the liquid without particles. Image taken from [86].

Hydrodynamic asymmetry has also been used to separate particles based on size. In pinched flow fractionation, a fluid with particles and a fluid without particles are injected into inlets that lead to a pinched channel. Based on the relative flow rates of the two fluids, particles are focused along one sidewall in the pinched channel. When the pinched region broadens into wider channel, large particles experience a force from the expanding flow toward the center of the channel while smaller particles are directed toward the channel walls [86]. Geometric asymmetry has been shown to enhance this effect [80], and pinched flow fractionation has also been applied to separation of cancer cells from leukocytes [66].

60

4.2.4 Centripetal Acceleration and the "Slingshot" Effect

As a particle follows a straight streamline, it is pushed by a viscous drag force, F_D, parallel to its motion, so that it moves at a velocity, v_p, equal to that of the fluid, v_f.

$$F_D = 6\pi\mu v_p R_p \tag{4.4}$$

where μ is the dynamic viscosity of the fluid and R_p is the radius of the particle.
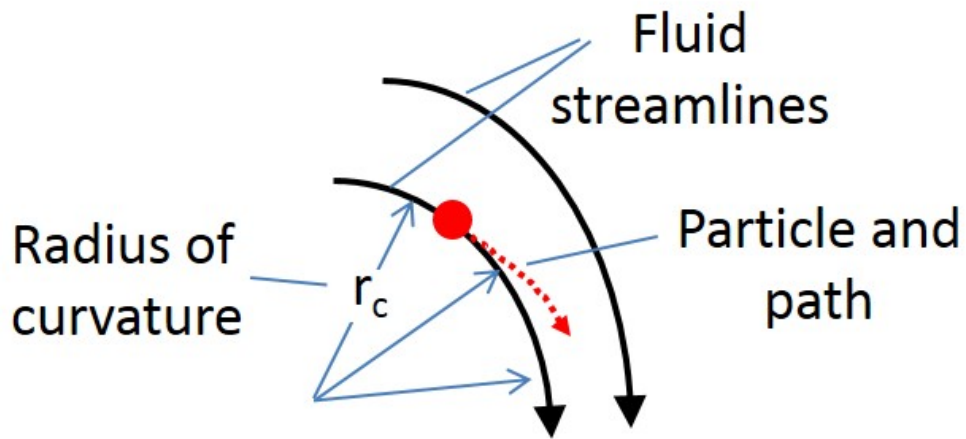
Figure 4.3: Qualitatve picture of a particle moving to an adjacent streamline when the fluid flow undergoes curvature.

When the streamline curves, if the particle were to follow the streamline, a centripetal force, F_C, would be required to cause the needed centripetal acceleration a_C:

$$F_C = (\rho_p - \rho_f)V_p a_c \tag{4.5}$$

where ρ_p and ρ_f are the particle and fluid mass densities, respectively, and V_p is the volume of the particle, and

$$a_c = v_p{}^2/R_c \tag{4.6}$$

where R_c is the radius of curvature.

Because of its inertia, the lack of an actual centripetal force will cause a particle denser than the fluid to move to an adjacent stream of greater radius, where the drag force will then cause the particle to accelerate along the new streamline (Figure 4.3) until the new streamline curves and the process repeats. Thus the particle will repeatedly be moving to outside streamlines when the fluid streamlines curve. We refer to this informally as the "slingshot" effect. Because the required centripetal force is proportional to the square of the velocity, this effect of moving particles across streamlines at curves is expected to increase as the flow rate increases.
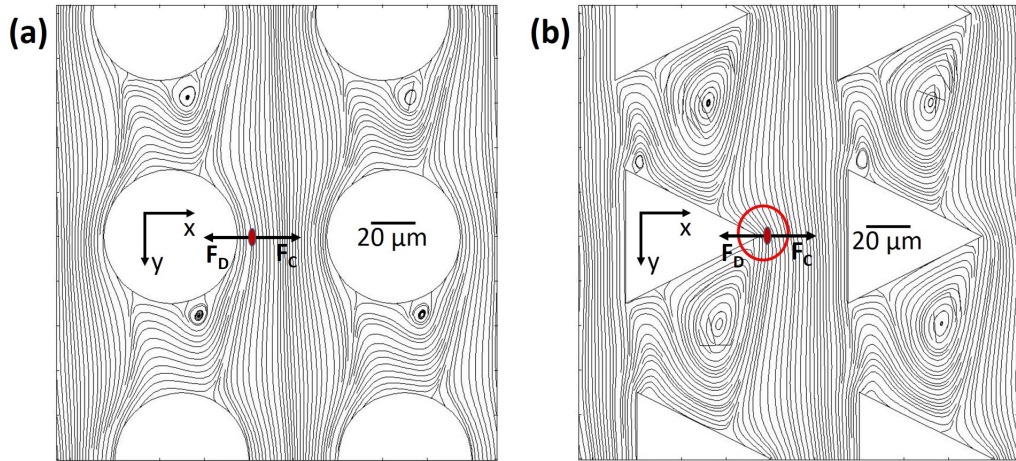
Figure 4.4: (a) Plot of streamlines in a DLD array with 60 μm circular posts, 40 μ gaps, and 1/20 tilt, and flow velocity corresponding to Re of 20. (b) Plot of streamlines in a DLD array with 60 μm asymmetric isosceles triangular posts, 40 μ gaps, and 1/20 tilt, and flow velocity corresponding to Re of 20. Note the sharp curvatures in the gap region with asymmetric triangular posts is circled in red in (b) compared to the curvatures with circular posts in (a).

We expect this process to depend on the post shape because different post shapes result in different curvatures of the streamlines, especially in the gap. Note in Figure 4.4 that the curvatures of streamlines in the gap can be much sharper for posts with sharp points in the gap (Figure 4.4(b)) than those for posts with smooth edges, such as circular posts (Figure 4.4(a)). If the velocities in the two gaps were the

same, the required centripetal forces for particles to follow streamlines and not move to adjacent streamlines would be much larger for the posts with sharp points, as in Figure 4.4(b).

We now describe an approach to quantitatively estimate how much this effect might be expected to move a particle laterally across streamlines. We assume the effect is "small, so that the particle does approximately follow a streamline over short distances, even with curves. At each point along its path, there is some small motion perpendicular to the streamline at curves, because of the lack of a centripetal force. This we can estimate by assuming the small motion perpendicular to the streamline leads to a drag force on the particle in that direction, equal to the centripetal force which would be needed to keep the particle on the streamline. We define v_L as the lateral velocity (perpendicular to the streamline). Starting with:

$$F_C = F_D \tag{4.7}$$

$$(\rho_p - \rho_f)V_p a_c = 6\pi\mu v_L R_p \tag{4.8}$$

and solving for the lateral velocity, v_L, yields:

$$v_L = \frac{(\rho_p - \rho_f)V_p a_c}{6\pi\mu R_p} \tag{4.9}$$

From the lateral velocity, we can find the distance perpendicular to the streamline that the particle has traveled due to the centripetal acceleration force, x_L, by integrating over the streamline path approximately traced by the particle:

$$x_L = \int v_L d(\frac{y}{v_y}) \tag{4.10}$$

where y is the distance in the average flow direction and v_y is the velocity in the average flow direction. These calculations are carried out numerically for erythrocytes for different post shapes at high Reynolds number in Section 4.5.3.

4.2.5 Effects on Cell Shape

Two effects become important as the flow rates, and correspondingly Re, at which DLD arrays are operated increases. First, the shear on the cells as the cells pass between the micro-posts increases, causing deformation of the cells that reduces the effective size of the cells [4]. This reduction of the effective size of the cells can be sufficient to change the behavior of the cells in the DLD array [68, 87]. Second, at high flow rates, certain post geometries displace erythrocytes, which are well below the critical sizes of the arrays in these cases [88, 70].

Shear Stress on Spheroid Cells (Leukocytes and Cancer Cells)

Deformable spheroid cells have been shown to assume an elongated shape at high shear rates (Figure 4.5), which leads to cells navigating through the DLD array as if the cells have smaller effective radii [4]. Thus, target cells to be harvested are not displaced into the product if the effective radii of these cells falls below the critical size of the array. Compared with cancer cells, leukocytes are deformed more for the same shear in a DLD array than cancer cells [41], and the deformability of leukocytes is a critical parameter in scaling of DLD arrays for high-throughput separation of leukocytes from large volumes of blood [37].

As the flow rate increases, the shear the cells experience passing between the micro-posts increases. Shear-induced cell deformation typically results from fluid bending around the up-stream face of the micro-post on the side in the direction of the tilt [15]. Z. Liu et al. showed that shear-induced deformation of cancer cells is significantly less with triangular posts compared with circular posts at high flow
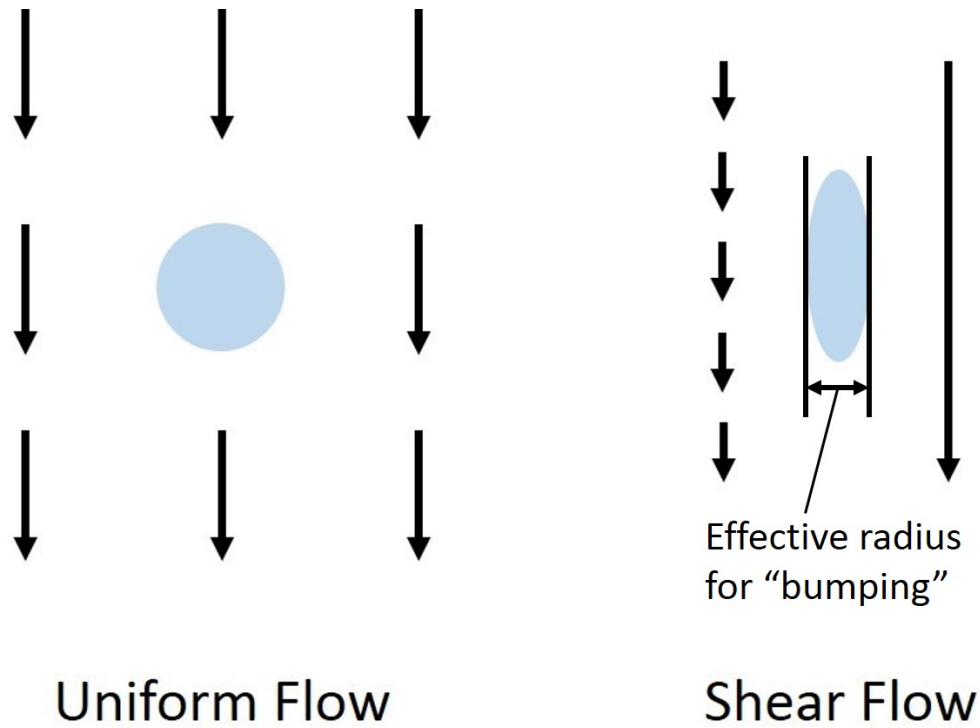
Figure 4.5: Spheroid cell of a given size (light blue) is not deformed in a uniform flow, but in a shear flow, is deformed significantly, with a decreased width (size along axis perpendicular to the flow) and increased length (size along axis parallel to the flow).

rates [47]. Recently, D. Holmes et al. demonstrated that leukocytes can be separated into subpopulations based on a combination of size and deformability in DLD arrays using circular posts [28]. M. Al-Fandi et al. developed a theoretical model for shear-induced compression of cells against the micro-posts in a DLD array and proposed diamond and airfoil shaped micro-posts to minimize this compression [1]. However, the effect of post geometry on shear-induced cell deformation has not been examined experimentally.

High Flow Rate Effects on Discoid Cells (Erythrocytes)

Hydrodynamic effects on the behavior of erythrocytes in DLD arrays are particularly interesting because erythrocytes are discoid in shape. J. Beech et al. have shown

that in deep channel DLD arrays (e.g. $>20\ \mu$m deep), such as the ones we use in our experiments, the shear causes the erythrocytes to align such that the long axis is parallel to the flow, and the erythrocytes behave as spherical particles with a diameter equal to the smallest dimension [4]. This alignment occurs to minimize the cross-section of the erythrocyte that is exposed to viscous drag from the flow. Recently, K.K. Zeming et al. and S. Ranjan et al. have shown that post geometry can be used to induce flipping (90° rotation) of the aligned erythrocytes, causing the erythrocytes to behave as particles larger than the critical size of the array even in deep channel DLD arrays [88, 70]. Because the major advantage of DLD arrays over other microfluidic technologies is the ability to separate nucleated cells from whole blood without the background of erythrocytes, characterizing the behavior of erythrocytes in DLD arrays with respect to post geometry at high flow rates is very important.

With this as background, we now go on to describe experiments and modelling to understand the behavior of erythrocytes and leukocytes in DLD arrays with different post shapes at high Re. These results are quite unexpected, and we show with optimal post shape that we can harvest leukocytes efficiently without substantial erythrocyte contamination.

4.3   Array Structure, Post Shapes, Experimental Conditions, and Modelling Approach

In this section, we discuss the array structure, post shapes, experimental conditions, and modelling approaches that we use in this chapter.

4.3.1 DLD Arrays for Separation of Nucleated Cells from Whole Blood
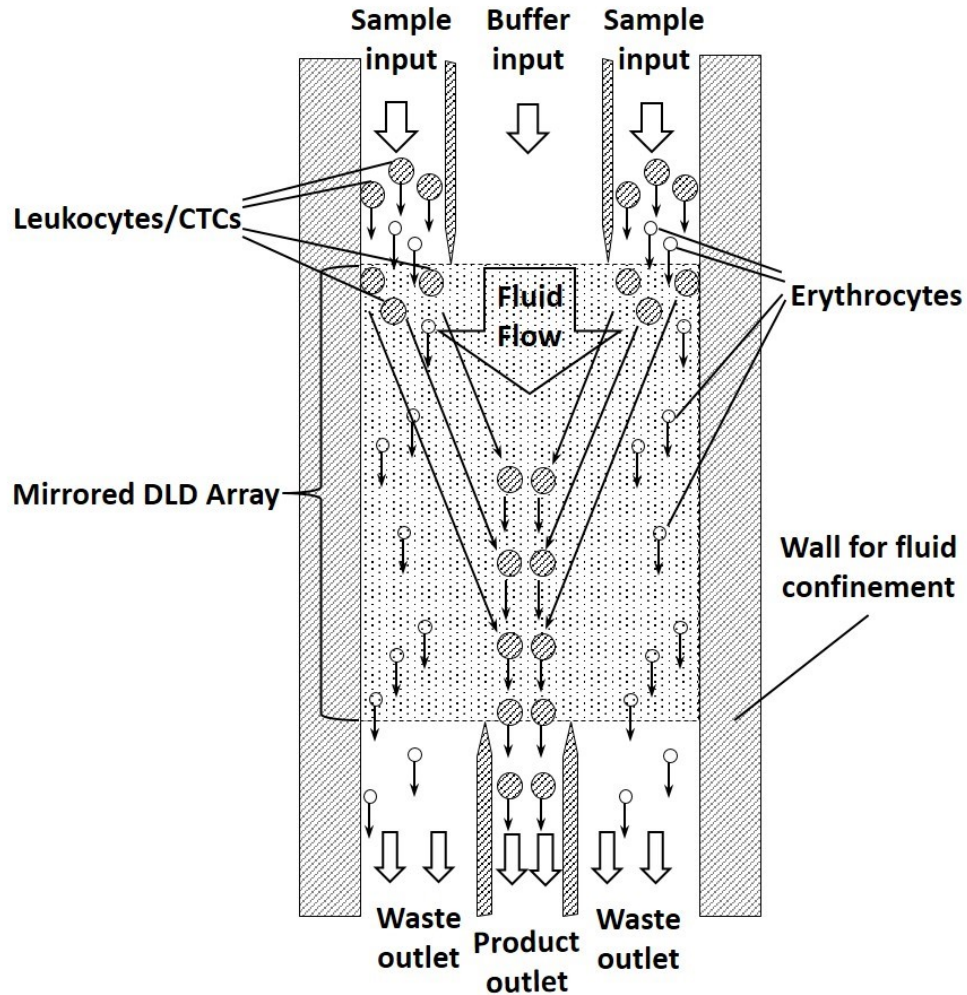
Figure 4.6: Schematic of the DLD array design used for separation of nucleated cells, such as leukocytes or PC3 cancer cells, from whole blood. The DLD array is a mirrored design in which sample enters at the outer sides of the array, and cells larger than the critical size are displaced toward the center of the array, in which buffer alone is input. The buffer input spans 9/19 the total width of the array, and each of the sample inputs span 5/19 the total width of the array. The product is collected at the end of the array from a width spanning 3/19 of the array width, and each of the waste outlets span 8/19 the total width of the array.

In order to capture leukocytes or cancer cells in a product free from non-target cells present in blood, we use a three-input mirrored DLD array (Figure 4.6). Blood

sample enters the array through inlets connected to the right and left sides of the array, while buffer enters the array through inlets connected to the center of the array. Target cells larger than the critical size of the array are displaced toward the center of the array into the buffer stream and are then collected through the product outlet, which spans 3/19 the total width of the array.
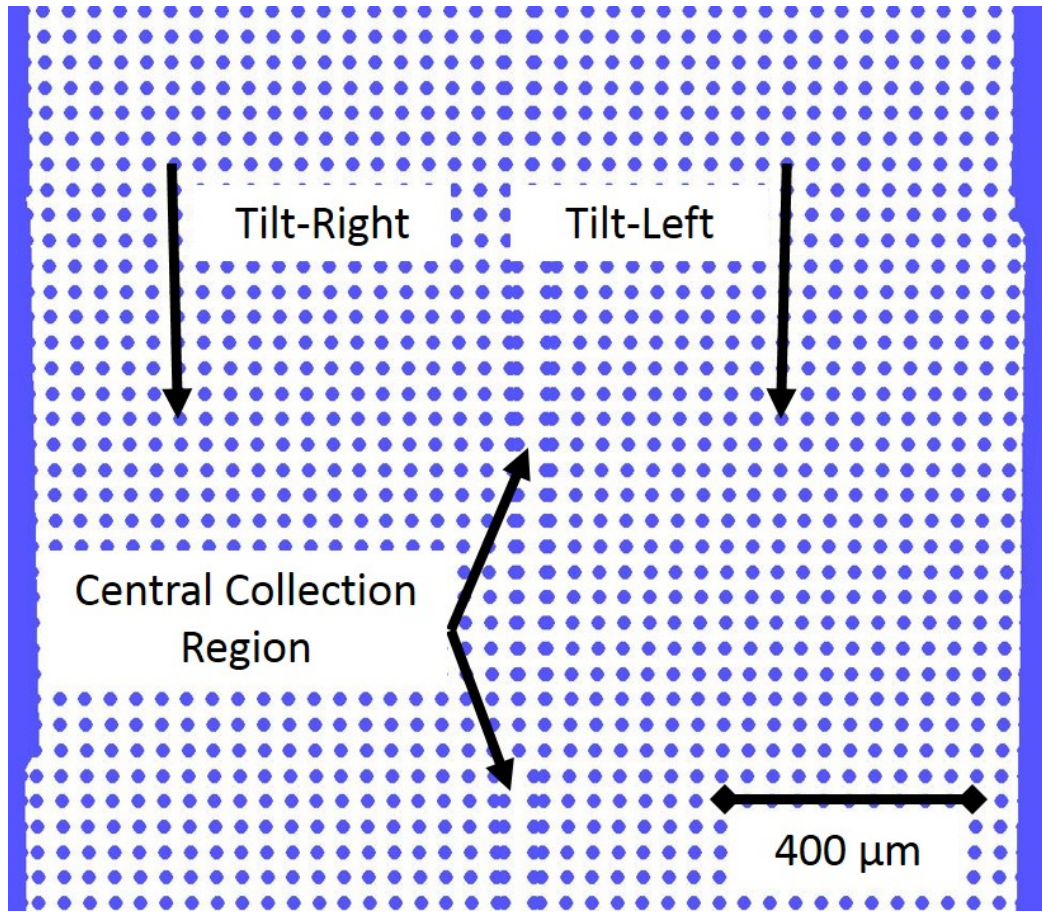
Figure 4.7: Schematic of mirrored array with circular posts for collection of leukocytes. The tilt on the left side of the array is to the right, and the tilt on the right side of the array is to the left. This displaces cells above the critical size of the array toward the center from each side. Instead of a wall in the middle, we use a fluidically balanced central collection region.

Mirrored DLD arrays have typically been designed to collect cells above the critical size of the array using a central wall [47, 50] that is fluidically balanced to maintain vertical flow even near the wall using the method developed by D. Inglis [34]. However,

adhesion of cells, particularly leukocytes, along this central wall is problematic in maintaining high capture efficiency for large volumes of blood. We instead use a fluidically balanced central collection region instead of a wall to capture displaced cells in the DLD arrays used in our experiments to avoid this problem (Figure 4.7).

Our experiments are conducted using DLD arrays reactively-etched in silicon to a depth of 160 μm by an anisotropic deep reaction ion etching (DRIE) process. The array is lidded with a 1-mm-thick Pyrex glass slide anodically bonded to the silicon chip into which the DLD array has been etched. The lidded device is mounted in an acrylic manifold to which fluidic connections are made via O-rings. A dual-syringe pump is used to drive buffer and sample (diluted blood) through the chip. Flow velocities in the array are reported as the syringe volumetric flow rate divided by the cross section formed by the depth of the channel (160 μm) and the gap between the posts (36 μm for cancer cell experiments, 17 μm for leukocyte experiments) times the number of gaps through which the fluid is flowing (23 for cancer cell experiments, 41 for leukocyte experiments) for a total effective width of 2.3 mm for cancer cell experiments and 1.5 mm for leukocyte experiments. This gives the average flow velocity in the gap, which is used along with the gap size as the characteristic length to calculate the Reynolds number.

Blood used in the experiments is obtained from Interstate Blood Bank (Memphis, TN), and experiments are conducted within 36 hours of the time the blood is drawn. Blood is diluted 1:3 in a buffer of PBS, 1% BSA (1%=1g BSA per 100 mL PBS), 5mM EDTA, and 40μM PPACK to inhibit clot formation [18]. The running buffer into which the leukocytes are collected is composed of PBS and 1% BSA.

4.3.2 Post Shapes and Array Parameters

The post shapes and critical sizes for the leukocyte yield and erythrocyte product contamination experiments and modeling are shown in Tables 4.1 and 4.2 below.

The critical sizes for circular posts are computed using the well-known experimental fit for critical size in circular post arrays with shallow tilt ($<1/10$) angles:

$$D_c = 1.4G\epsilon^{0.48} \tag{4.11}$$

where G is the gap size and ϵ is the tilt angle of the array [15].

For arrays with asymmetric isosceles triangular posts with shallow tilt ($<1/10$) angles, based on theory by K. Loutherback et al. [49], we propose a similar fit for critical size:

$$D_c = 1.0G\epsilon^{0.48} \tag{4.12}$$

This fit agrees well with experimental results with polymer microsphere beads (3 μm, 6 μm, and 10 μm), leukocytes, and PC3 cancer cells for asymmetric isosceles triangular post arrays with tilts of 1/20, 1/26, 1/36, and 1/42.

The critical sizes for all post geometries are first computed at the stated Re by the method proposed by D. Inglis et al. [35] using the velocity profile generated by the 2D laminar flow module in COMSOL. Fundamentally, this method examines the width of the streamline next to the post, as shown in Figure 1.1. This is done with an array with posts that can fit within a 60 μm by 60 μm square, 40 μ gaps, and 1/20 tilt. The critical sizes for symmetric post shapes (including quarter circle and semi-circle) are then scaled to the appropriate gap and tilt using the experimental fit for circular posts. The critical sizes for asymmetric post shapes are scaled to the appropriate gap and tilt using the experimental fit for asymmetric triangular posts.

Leukocyte Yield Experiments

The post shapes and critical sizes used for the leukocyte yield experiments are shown in Table 4.1.

Table 4.1: Post shapes used in the leukocyte yield experiments. Experiments are conducted at a flow velocity corresponding to Re of 2.3, with the average velocity in the gap between the posts being 13.5 cm/s. Array parameters are posts that can fit within a 19 μm by 19 μm square, 17 μm gaps, and 1/42 tilt, except for the asymmetric isosceles triangle, which has posts with 34 μm height and width, 22.5 μm gaps, and 1/42 tilt.

Tilt | Post | Flow	Geometry	Critical Size (μm) at Re = 2.3
	Asymmetric Triangle	3.8
	Circle	4.0
	Quarter Circle	4.0
	Rhombus	4.2
	Symmetric Triangle	4.0
	Diamond	3.5

The first column shows the post shape as oriented with respect to the flow, which is vertical. For the orientation of posts shown in Table 4.1, the tilt of the array is to the right, meaning each subsequent row is offset 1/42 of a horizontal period (period = post + gap = 36 μm). Thus, the unit cell of the array is rhombic with interior angles of 90°+/-1.36°. In the actual mirrored array (Figure 4.6 and Figure 4.7), the right half of the array, which has tilt to the left, has posts that are flipped horizontally with respect to those shown in Table 4.1.

We define symmetry about the center of the gap with respect to an axis parallel to the average flow direction. Thus, the asymmetric triangle is asymmetric by this definition, just as the symmetric triangle is symmetric. Also, note that the rhombus

has interior angles of 90°+/-2.72°, with two sides perpendicular to the average flow direction and the other two sides at an angle of 1.36° relative to the tilt angle.

The variation in the critical size with post shape in Table 4.1 is mainly a result of the effect of the post shape on the velocity profile in the gap and to a lesser extent an effect of increasing Re on the velocity profile in the gap. The critical size is still significantly larger than the expected 2.5 μm size of erythrocytes for a deep-channel (depth>20 μm). The maximum flow velocity and Re at which experiments can be conducted is limited by the maximum force which the syringe pump can apply, and average flow velocity in the gap of 13.5 cm/s and Re of 2.3 are currently the maximum achievable for an array with 17 μm gaps. The fluidic resistance of the array scales with the square of the gap width, so significantly higher flow velocities and Re can be achieved in arrays with a larger gap width.

Erythrocyte Product Contamination Experiments

The post shapes and critical sizes used for the erythrocyte product contamination experiments are shown in Table 4.2, which is similar in layout to Table 4.1.

We seek to examine post-shape-dependent erythrocyte contamination of the product over a wider range of flow rates (velocities) and Re than we examine for post-shape-dependent compression of leukocytes. The limitation on the maximum flow rate we can operate the DLD array is determined by the maximum pressure that can be supplied by the syringe pump divided by the fluidic resistance of the array. The fluidic resistance of the array scales inversely with the square of the width of the gap between the posts. Thus, we use arrays with the array parameters that were used in the cancer cell harvesting experiments in Chapter 3 to examine the dependence of erythrocyte contamination of the product on post shape at Re up to 15, corresponding to an average flow velocity in the gap of 42.9 cm/s.

Table 4.2: Post shapes used in the erythrocyte product contamination experiments. Experiments are conducted at a flow velocity corresponding to Re of 15, with the average flow velocity in the gap between the posts being 42.9 cm/s. Array parameters are posts that can fit within a 62 μm by 62 μm square, 36 μm gaps, and 1/26 tilt for all post geometries.

Tilt | Post | Flow	Geometry	Critical Size (µm) at Re = 15
	Asymmetric Triangle	7.6
	Circle	10.0
	Rounded Triangle	7.8
	Extended Semi-Circle	9.3
	Upright Triangle	7.8
	Quarter Circle	10.0
	Downturned Triangle	7.1
	Square	11.4

4.3.3   Modelling of Flow Streamlines

Modelling is performed in the numerical simulator package, COMSOL, using the 2D laminar flow module. All simulations are performed with array parameters of 60 μm posts, 40 μm gaps, and 1/20 tilt. The array size is 700-μm width (perpendicular to the flow direction) and 2-mm length (parallel to the flow direction). The walls of the array are designed to preserve vertical flow near the edge of the array [34]. Boundary conditions are "no slip" at the walls of the array and the edges of the posts. The flow rate is controlled by the normal inflow velocity across the top boundary of the array

(i.e. constant flow per unit width). Fluid properties (density and dynamic viscosity) are that of water at room temperature: density of 1 kg/m^3 and dynamic viscosity of 1x10^{-3} kg/(m·s). Disturbance of the fluid by particles and any possible inertial effects depending on variations in channel depth are not included in the simulation. Further details about the simulations performed in this chapter can be found in Appendix E.
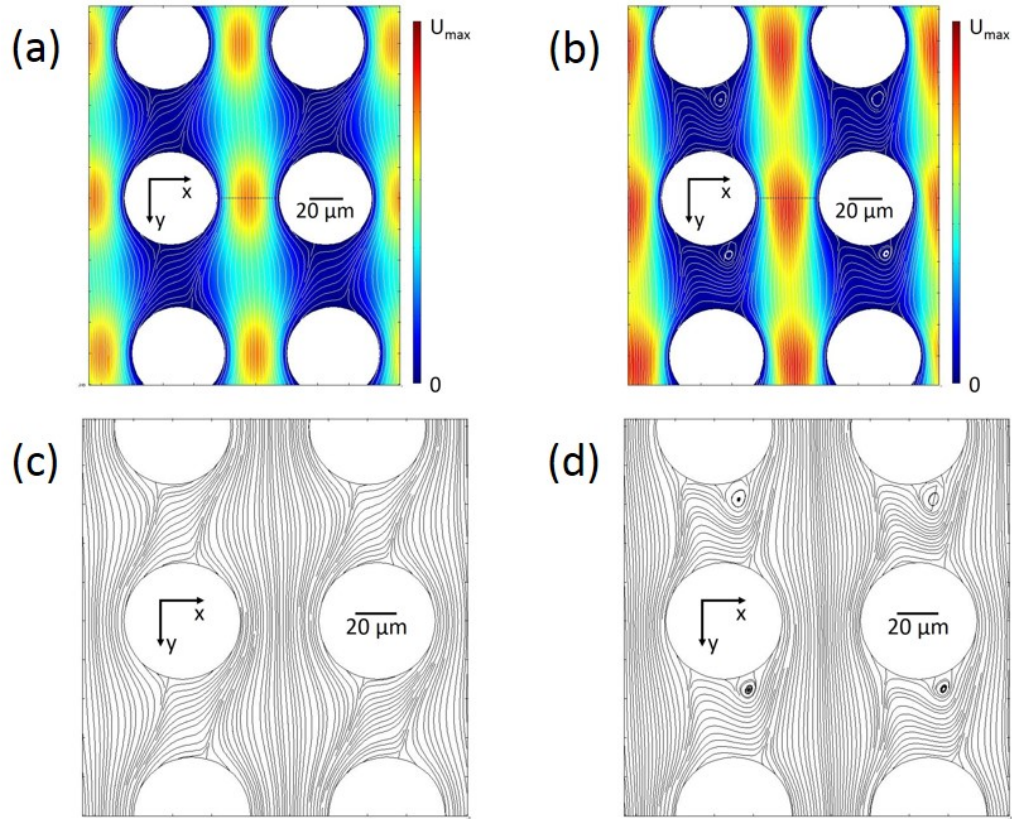

Figure 4.8: Surface plots of fluid velocity and streamlines in a DLD array with 60 μm circular posts, 40 μm gaps, and 1/20 tilt at Re of (a, c) 1 and (b, d) 20. Note the elongated high velocity region in the gap and the vortices behind the posts at Re of 20.

Figure 4.8 shows surface plots of the fluid velocity and streamlines in a DLD array with 60 μm circular posts, 40 μm gaps, and 1/20 tilt at Re of 1 and 20. Some qualitative conclusions can be drawn from Figure 4.8. As Re increases, the high velocity region in the gap becomes elongated because of the fluid's inertia in the high velocity gap region. The fluid does not like to spread out in the broadening region

between the posts at high Re, and at Re>10, vortices behind the posts form for this reason. The increased flow velocity increases the fluid shear as the fluid bends around the bumping side of the post into the gap. In section 4.4, we discuss how this contributes to cell compression against the posts and how certain post shapes minimize this effect. It has been suggested that the vortices that form at Re~10 prevent particles below the critical size from behaving in zig-zag mode, thus making these particles behave as particles above the critical size of the array [56, 54]. We use the streamlines and detailed flow pattern extensively in explaining the behavior of erythrocytes as Re increases beyond 1 in section 4.5.

4.4 Leukocyte Yield and Post Shapes at High Flow Rates
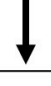
In this section, we experimentally determine and fundamentally explain how post shape affects leukocyte yield at high flow rates.

4.4.1 Experiment and Results

We use arrays with parameters described in Table 4.1 to separate leukocytes from whole blood. The length of the array is 39.3 mm, and the total array width is 1.5 mm. The experimental conditions at which leukocyte capture is measured are (i) the average flow velocity in the gap is 13.5 cm/s, the Reynolds number (gap width * average flow velocity in the gap / kinematic viscosity of water at room temperature) is 2.3, and (ii) the average shear rate (average flow velocity in the gap / half the width of the gap) is 15000 s^{-1}. The results for the six post geometries tested are shown in Table 4.3 below.

Although the critical sizes for all of the post shapes are similar (Table 4.1), the leukocyte yields vary strongly based on post shape. The leukocyte yields vary from

Table 4.3: Leukocyte yield (harvested into the central product outlet) for different post geometries under the same experimental conditions. Array parameters are 19 μm posts, 17 μm gaps, and 1/42 tilt for all post geometries except the asymmetric triangle, which has 34 μm posts, 22.5 μm gaps, and 1/42 tilt. The average flow velocity in the gap is 13.5 cm/s, the Reynolds number is 2.3, and the average shear rate is 15000 s^{-1} for all post geometries. Volume of blood was greater than 3 mL for each post shape, and blood was diluted 1:4. The running time ranged from 30 to 40 minutes for each post shape.

Tilt	Post	Flow	Geometry	Leukocyte Yield (%)
↘	▷	↓	Asymmetric Triangle	81.3
↘	●	↓	Circle	25.2
↘	◖	↓	Quarter Circle	18.7
↘	■	↓	Rhombus	32.9
↘	▲	↓	Symmetric Triangle	64.8
↘	◆	↓	Diamond	83.6

18.7% to 83.6%. Leukocyte yields for post shapes with relatively flat surfaces parallel to the flow in the gap are significantly lower than the leukocyte yields for post shapes with vertices facing into the gap. The circle and quarter circle (quarter circle with rounded edge facing upstream and on the bumping edge) post geometries resulted in less than 30% of leukocytes being displaced into the product. This low yield is a high Re effect as the leukocyte yield was 88% using a nearly identical DLD array with circular posts (18 μm posts, 18 μm gaps, 1/42 tilt, with critical size 5% greater than the circular post array used in the experiment in Table 4.3) operated at Re of 0.07, corresponding to an average flow velocity in the gap of 0.4 cm/s.

Although offering less surface area against which the leukocytes could be compressed compared to circular and quarter-circular posts, rhombus-shaped posts displaced only 32% of the leukocytes into the product. Posts with sharp corners facing into the gap had much higher leukocyte yields, with symmetric isosceles triangles displacing 64% of erythrocytes into the product and asymmetric isosceles triangular posts and diamond posts displacing more than 80% of leukocytes into the product.
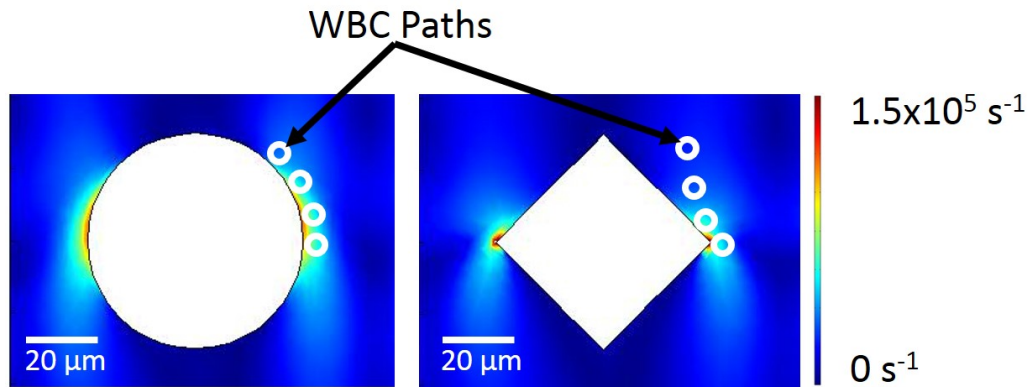
4.4.2 Modelling

Figure 4.9: Surface plot of the shear rate around a circular post (left) and a diamond post (right) in a DLD array with the flow having a Re of 15. Flow direction is from top to bottom, and the array tilt is to the right. Note that there is a significantly larger high-shear region on the right and left sides of the circular post compared to the diamond post. Cell compression occurs in the high-shear region on the upstream facing half of the right (bumping) side of the post, as a cell in the first streamline next to the post follows the streamline around the post. The white circles qualitatively represent a leukocyte (WBC) path following the first streamline around the bumping side of the post.

We hypothesize that the low yield of leukocytes is due to shear stress elongating the cells, so the cells act "smaller" than expected and below the critical size for bumping (See Section 4.2.5 and Figure 4.5). The shear rate is the rate at which a progressive shearing deformation is applied to the fluid, in this case, by the walls of the micro-posts and can be represented in a 2D coordinate system by:

$$\gamma_{ij} = \frac{\partial v_i}{\partial x_j} + \frac{\partial v_j}{\partial x_i} \qquad (4.13)$$

where v_i and v_j are the velocities in the i and j directions, respectively, and x_i and x_j are the displacements in the i and j directions, respectively.

We now examine the shear rate around micro-posts of various shapes in a DLD array with micro-posts with height and width of 60 μm, gaps of 40 μm, and tilt of 1/20 in a flow having Re of 15 using the 2D laminar flow module in COMSOL (Figure 4.9). Qualitatively, the shear rate is a measure of the extent to which the fluid bends around the post. There is a significantly larger high shear rate region on the right (bumping) and left sides of the circular post compared with the diamond post (Figure 4.9). This means that the fluid, in bending around the post, interacts far more with the circular post than with the diamond post, and a cell following this fluid will correspondingly interact (be deformed) more by a circular post than by a diamond post, as can be seen from the path followed by the leukocytes in Figure 4.9. The cell interaction with the diamond post is more of a glancing blow, whereas with a circular post, the interaction is a more sustained deformation.

The shear rate near a micro-post in a DLD array is highly dependent on post geometry. For shallow tilt angles (tilt < 1/10), the shear rate is sensitive primarily to post shape, and there is little qualitative dependence on post size, gap size, or Re (for Re>1), as long as these are maintained to fixed values when comparing among post shapes. There is a significantly larger high shear region on the sides parallel to the flow direction of a circular post compared with a diamond post (Figure 4.9) or a triangular post. This high-shear region results from fluid bending around the micro-post, leading us to examine the relationship between the shear from the fluid bending around the micro-post to the extent of cell deformation.

The shear rate of the fluid at the surface of the micro-post comes from two sources. The first is that the fluid velocity is constrained to zero at the surface of the micro-
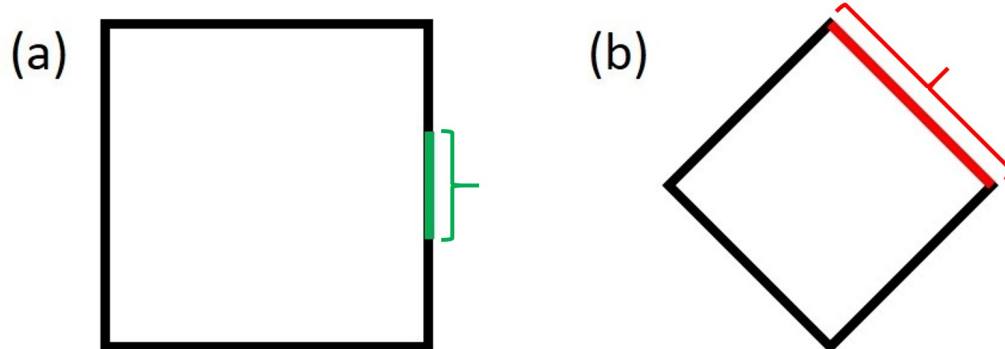
Figure 4.10: (a) Average shear rate in the region highlighted and bracketed in green is used to determine the shear rate of the fluid at the surface of the post that results from the vertically flowing fluid being confined to the gap such that the fluid velocity at the wall of the post is zero. (b) The shear rate less the average shear rate calculated in (a) is integrated along the length of the line highlighted and bracketed in red to determine the shear from the fluid bending around the post that contributes to cell compression. The region highlighted in red is the region where a cell can be compressed for an array in which the tilt is to the right and the flow is from top to bottom.

post, while it has some finite velocity in the gap. An upper bound for the shear rate from this source at a given flow rate can be found by taking the average value of the shear rate in the region highlighted in green for a square post as shown in Figure 4.10(a). The second source, which results in significantly higher shear rates, is from the fluid bending around the micro-post. The region in which the shear rate from this source contributes to cell compression is highlighted in red in Figure 4.10(b) and can more generally be described as the region at the surface on the bumping side of the post that has an outward normal that points between 0° and 90° on a standard unit circle, where 0° points from the bumping side of the post into the gap perpendicular to the average flow direction. In other words, it is the upstream edge on the side where the particle will "bump" against the post.

We integrate the shear rate from the fluid bending around the micro-post over the region at the surface of the micro-post against which cell compression can occur. We define the shear rate from the first source described above as γ_0 and the total shear rate as γ. For each micro-post shape, we then compute:
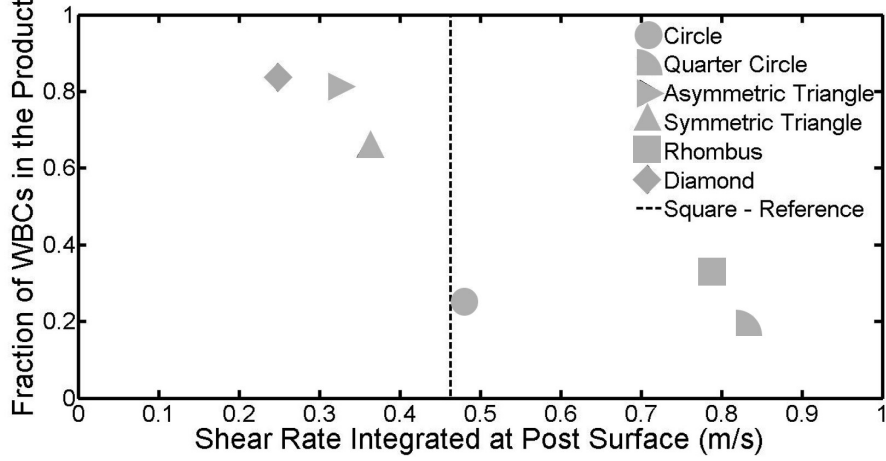
Figure 4.11: Fraction of leukocytes displaced into the product as a function of the shear rate from fluid bending around the micro-post integrated over the surface of the micro-post at which cell compression can occur for six different post geometries. The shear rate from fluid bending around a square micro-post integrated over the surface of the micro-post against which a cell can be compressed is shown for reference. The shape of the posts is schematically indicated, assuming the flow direction is vertical from top to bottom. The tilt of the array is to the right as one moves down through the array, and the flow is from top to bottom.

$$\int_L (\gamma(s) > \gamma_0) \cdot (\gamma(s) - \gamma_0) \cdot ds \qquad (4.14)$$

where L is along the edge of the post against which a cell can be compressed and integration only occurs for $\gamma(s) > \gamma_0$. The integral is computed for each of the six post geometries using the model described in Section 4.3.3 and compared to the experimental results from Section 4.4.1 in Figure 4.11.

From Figure 4.11, we see that leukocyte yield is inversely related to the shear rate at the surface of the post integrated over the surface against which the cell can be compressed. Since we are only integrating along the surface of the post, this means that the area of the "bumping" surface of the post that contributes to fluid bending around the post is significant. Posts with vertices (sharp corners) facing into the gap result in cells experiencing a glancing blow against the post, resulting